A SIMULATION STUDY OF TERAHERTZ QUANTUM WELL PHOTODETECTOR AT 3 THZ

Mahmoud ALMASSRI

Master of Science Thesis

Department of Physics

Programme in Solid-state physics

Supervisor: Prof. Dr Yüksel ERGÜN

Eskişehir

Eskişehir Technical University

Institute of Graduate Programs

December 2020

ABSTRACT

A SIMULATION STUDY OF TERAHERTZ QUANTUM WELL PHOTODETECTOR AT 3 THZ

Mahmoud ALMASSRI

Department of Physics

Programme in Solid-state physics

Eskişehir Technical University, Institute of Graduate Programs, December 2020

Supervisor: Prof. Dr Yüksel ERGÜN

In the last few decades, scientists have been rapidly developing new techniques to exploit the THz part of the spectrum, and with development of fast and reliable THz sources like THz Quantum Cascade Laser, the need to develop fast and reliable THz detectors became obvious and urgent, and the THz QWP is one of the best candidates to fill this gap.

This thesis reports a new THz quantum well photodetector with peak frequency operation of about 3.1 THz and presents a simulation study for the potential profile, the absorption coefficient and the dark current of the device using a developed MATLAB simulations that have been tested by replicating previously published results in the literature.

Keywords: AlGaAs/GaAs, QWIP, THz, Intersubband transitions, Dark current.

ÖZET

3 THZ'DE TERAHERTZ KUANTUM KUYUSU FOTODETEKTÖRÜNÜN SIMÜLASYON ÇALIŞMASI

Mahmoud ALMASSRI

Fizik Anabilim Dalı

Katı hal fiziği Bilim Dalı

Eskişehir Teknik Üniversitesi, Lisansüstü Eğitim Enstitüsü, Aralık 2020

Danışman: Prof. Dr Yüksel ERGÜN

Son birkaç on yılda, bilim adamları, spektrumun THz kısmını kullanmak için hızla yeni teknikler geliştiriyorlar ve THz Quantum Cascade Laser gibi hızlı ve güvenilir THz kaynaklarının geliştirilmesiyle, hızlı ve güvenilir THz dedektörleri geliştirme ihtiyacı açık ve acil hale geldi ve THz QWP bu boşluğu doldurmak için en iyi adaylardan biridir.

Bu tez, yaklaşık 3,1 THz'lik tepe frekansı işlemine sahip yeni bir THz kuantum kuyusu fotodedektörünü bildirir ve daha önce yayınlanmış olanların çoğaltılmasıyla test edilmiş gelişmiş bir MATLAB simülasyonları kullanılarak cihazın potansiyel profili, soğurma katsayısı ve karanlık akımı için bir simülasyon çalışması sunar. literatürde sonuçlanır.

Anahtar Sözcükler: AlGaAs/GaAs, QWIP, THz, Alt bantlar arası geçiş, Karanlık akım.

ACKNOWLEDGEMENTS

First and foremost, I would like to thank my supervisor Prof. Yüksel ERGÜN who was patient and very helpful throughout my Master studies. Without his guidance, this work would not have been done.

I would also like to thank Prof. MUSTAFA HOŞTUT from the Mediterranean University for helping me and sharing his research experience with me. Many thanks to my colleagues and my teachers at Eskisehir Technical University from whom I have learned a lot in the course of my master's studies.

Finally, I would like to express my great gratitude to my family for their support and encouragement during the years that I spent away from them.

Mahmoud ALMASSRI

30/12/2020

STATEMENT OF COMPLIANCE WITH ETHICAL PRINCIPLES AND RULES

I hereby truthfully declare that this thesis is an original work prepared by me; that I have behaved in accordance with the scientific ethical principles and rules throughout the stages of preparation, data collection, analysis and presentation of my work; that I have cited the sources of all the data and information that could be obtained within the scope of this study, and included these sources in the references section; and that this study has been scanned for plagiarism with "scientific plagiarism detection program" used by Eskişehir Technical University, and that "it does not have any plagiarism" whatsoever. I also declare that, if a case contrary to my declaration is detected in my work at any time, I hereby express my consent to all the ethical and legal consequences that are involved.

Mahmoud ALMASSRI

CONTENTS

Page

LIST OF TABLES

Page

LIST OF FIGURES

Page

GLOSSARY OF SYMBOLS AND ABBREVIATIONS

THz	:	Terahertz
QWIP	:	Quantum well infrared photodetector
QCL	:	Quantum Cascade Laser
MBE	:	Molecular Beam Epitaxy
ψ	:	Wave function
V_{xc}	:	Exchange-correlation potential
V_H	:	Hartree potential
I_{photo}	:	Photocurrent
I_{dark}	:	Dark current
α_{2D}	:	The two- dimensional absorption coefficients

1. INTRODUCTION

1.1. Exploiting the Terahertz (THz) range of the spectrum

The science and technology that targets to harness the Terahertz region of the electromagnetic spectrum, which lies in the range from ~0.1 THz to ~10 THz as shown in Figure (1.1), has been an active area for research in the last few decades (Mittleman, 2017). The research conducted in this field showed that the THz technology has potential applications in a wide variety of fields such as: security, material characterization, high speed telecommunication and medicine. Terahertz radiation is considered to have a low energy when compared to X-ray, and due to this advantage and its non-ionizing property, it is considered to be more environment friendly and a better imaging technology than using X-ray imaging (Pawar, Sonawane, Erande, & Derle, 2013).

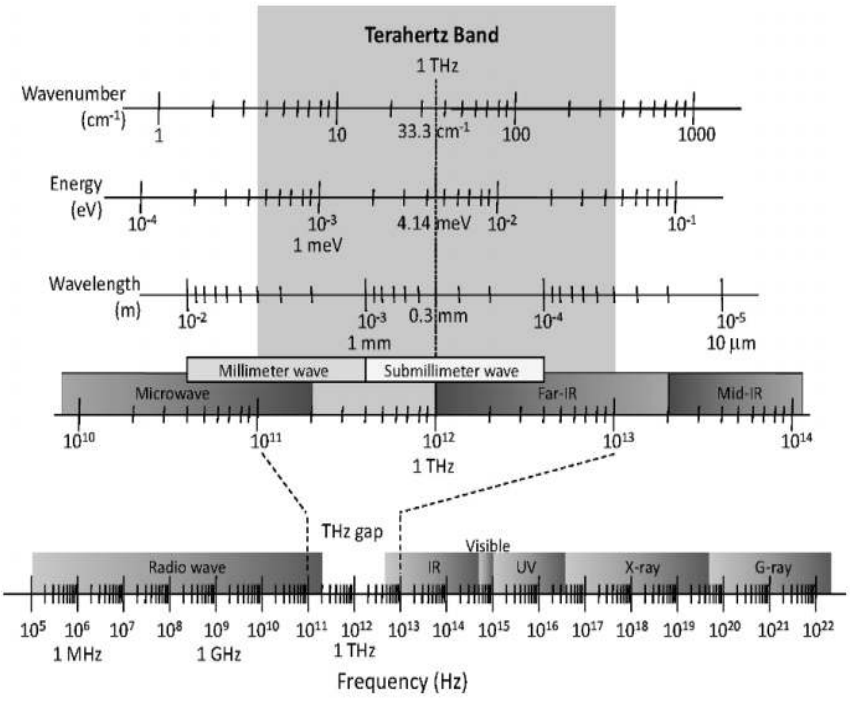

Figure 1.1. *Terahertz portion of the electromagnetic spectrum. The picture is taken from (Lee, 2009)*

In order to exploit the THz range in the most effective way, high response speed THz detectors and powerful THz sources must be developed. As a solution to the problem of the lack of powerful THz sources, the THz Quantum Cascade Laser (QCL) has been continuously developed over the last two decades, and the researches done in an effort to

enhance this device have proven it to be a powerful and efficient THz source. For example, the highest temperature performance published record is 210.5 K with a maximum output power of 200 mW (Bosco et al., 2019). However, the other part of the mission that needs to be achieved to enable an extensive study and build reliable THz technologies is to develop fast THz detectors with high sensitivity, and THz Quantum Well Photodetectors are considered to be among the best candidates to fulfil this purpose and they have been in a consistent development since they firstly proposed by H.C.Liu in 2004 followed by a similar paper published by Graf et al in the same year (Graf et al., 2004; H. C. Liu, Song, SpringThorpe, & Cao, 2004).

However, although THz QWP has been continuously developed since then, a small number of studies has been done to develop THz QWPs that operate around a frequency of 3 THz or an energy of about 12.4 meV, and the main reason for that is that the Aluminum fraction in $AL_xGa_{1-x}As/GaAs$ THz QWP that works at low THz frequency is very small, which makes it difficult to achieve a high quality MBE growth. Hence, the motivation behind this thesis is to develop a theoretical model for a THz QWP that operates around 3 THz and to provide a simulation for the dark current and the absorption coefficient of the device.

1.2. Terahertz detectors

Scientists have realized the wide potential applications of THz technologies and extensive work has been done and still going on in order to develop a THz detector that has a high responsivity and able to operate at temperatures close to room temperature. Thus, different kinds of THz detectors have been developed and most of these detectors can be classified into two general categories, namely thermal detectors and photon detectors. The operation principle of THz thermal detectors is to absorb the energy of the incident THz radiation which leads to a change in the temperature of the device, then the change of some properties of the device's material leads to producing an electrical current. On the other hand, photon detectors work by generating photocurrent that results when electrons confined in a quantum well, or bound to an atom or free electrons, absorb

the energy of the incoming THz photons and get excited to a higher state and contribute to the photocurrent that flows in the device (Rogalski, 2017).

1.3. Semiconductor Heterojunctions

A Semiconductor heterojunction forms up when two semiconductors with different band gaps comes into contact. When two semiconductors with the same band gaps are connected, we have a band bending as in the p-n junction, however, an abrupt junction is formed when the two semiconductors are with different energy band gaps. With today's advanced growth methods such as molecular-beam epitaxy, the band gaps offset that characterizes the heterojunction can be controlled by growing different combinations of semiconductors to build optoelectronic and electrical devices that works by exploiting the different properties of the heterojunction, such as carriers confinement as in Quantum Well Heterostructures for example. According to how their band gaps align, semiconductor heterojunctions are classified into three types, as shown in Figure (1.2) (Brillson, 2016).

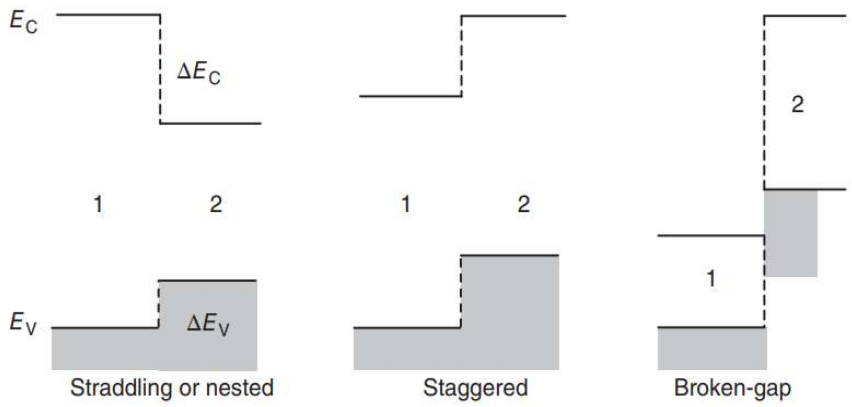

Figure 1.2. The three types of Semiconductor heterojunctions based on band gap alignment (Brillson, 2016).

Some resources refer to the straddling junction as type I, the staggered junction as type II and to the broken gap as type III heterojunction (or type-II staggered). And as shown in Figure (1.2), the main difference between the three types of the heterojunctions stems from the different lining up of the band gaps of material 2 with material 1.

1.3.1. Type I Heterojunction

In this type of heterojunctions, both the conduction and the valence bands of the semiconductor with smaller band gap lie between the conduction and the valence bands of the semiconductor that have the wider energy band gap. An example of this types of heterojunctions is the junction formed between $Al_xGa_{1-x}As$ and GaAs where the bands offset can be controlled by changing the aluminum fraction *x*. The difference in band gaps equals the sum of the conduction bands offset and the valence band offset, which can be described by the following equation

$$\Delta E_g = \Delta E_c + \Delta E_v \tag{1.1}$$

the conduction band offset can be written as follows

$$\Delta E_c = \chi' - \chi \tag{1.2}$$

Where χ' and χ are the electron affinities of the second and the first semiconductor respectively (Lundstrom, 1995).

1.3.2. Type II Heterojunction

In this type, the edge of the conduction band of the second material is located above the bottom of the conduction band of the first material, while the valence band of the second material lines up within the band gap of the first material. An example of types II of heterojunctions is the junction formed between $Al_xIn_{1-x}As$ and InP.

1.3.3. Type III Heterojunction

It is also called the broken gap heterojunction or type II misaligned heterojunction, and it forms when the conduction band of one material is located below the valence band of the other material, as shown in Figure (1.2). An example of this type is InAs/GaSb heterojunction (Lundstrom, 1995)

1.4. Quantum Well Infrared Photodetectors

Scientists have realized long time ago the possibility of constructing quantum wells by exploiting the heterostructures that form up between semiconductor materials with different energy band gaps. However, the development of growing methods such as Molecular-beam epitaxy made it possible to build these structures with high accuracy and high quality. Structure based on III-V materials are the most commonly used to build QWIPs, especially $Al_xGa_{1-x}As/GaAs$ quantum wells, where the first QWIP was demonstrated in 1987 and it was $Al_xGa_{1-x}As/GaAs$ based (Levine, Choi, Bethea, Walker, & Malik, 1987). The position of the energy subbands of the heterostructure quantum well and the difference between them can be controlled by changing the width of the well, the height of the barriers and it depends as well on the effective mass of the carriers. So, with maturity of energy level engineering, many successful models of QWIP that operate at different frequencies have been demonstrated over the last three decades (Schneider & Liu, 2007). The operating principle of QWIP depends on the Intersubband transitions that take place between the confined subbnds in the quantum well when an incident infrared radiation is absorbed by the confined carriers and excites them to a higher state allowing them contribute to a photocurrent that flows in the detector, where the active region of the detector is designed such that the energy difference between the subbands matches the energy of the radiation we would like to detect, as shown in Figure (1.3).

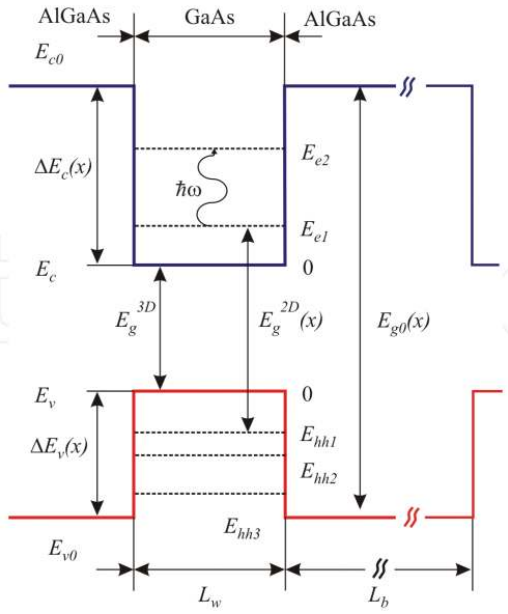

Figure 1.3. *Intersubband transitions of electrons and holes in AlGaAs/GaAs quantum well (Dem'yanenko et al., 2018).*

In the diagram shown in Figure (1.3), the electrons in the ground state E_{e1} can absorb the energy of the incident photons and get excited to the first excited state E_{e2} or to the continuum, which depends on the energy of the incident radiation. The positions of the confined subbands can be varied by changing the width of the well L_w and by increasing the height of the barriers, where the height of the barriers depends on the aluminum fraction in $Al_xGa_{1-x}As$. Another important parameter that needs to be taken into consideration when designing the active region of the QWIP is the width of the barriers, where their width is chosen to be much larger than the width of the quantum well, and that is to prevent electrons from tunneling through the barriers and cause dark current (Dem'yanenko et al., 2018).QWIP is a device that have multiple quantum wells (modules) like that shown in Figure (1.3), and the number of modules that make up the device depends on the quality of the growth process. If the first excited state is aligned with the top of the well, then when radiating gets absorbed by the electron in the ground state they become excited occupy the first excited state, and these electrons can easily move and create a photocurrent if a voltage bias is applied, as shown in Figure (1.4).

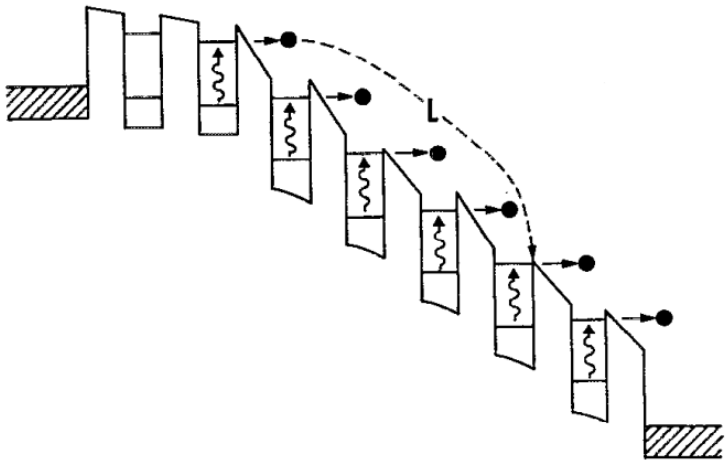

Figure 1.4. *A multiple Quantum Well Structure under voltage bias, where electrons absorb the incident radiation and get excited to the first excited state and contribute to the photocurrent (Levine, 1993).*

1.5. THz QWP

Scientists has been working and developing new techniques and devices to harness the THz portions of the spectrum for last few decades, and many Terahertz detectors have been developed for this purpose. The first THz QWP has been demonstrated by H.C.Liu in 2004 (H. C. Liu, Song, SpringThorpe, & Cao, 2004)), different studies have been done to develop different models of THz QWP's that operates at different response peaks and to improve other properties such as detectivity and decreasing the dark current, and these studies have proven that THz QWP's to be fast and reliable THz detectors (Castellano, Iotti, & Rossi, 2008; Guo, Cao, Zhang, Tan, & Liu, 2013; Jia, Wang, Zhang, & Schneider, 2015; X.-h. Liu, Liao, Zhou, Li, & Li, 2013; S. Zhang et al., 2013).

The most commonly used material system for THz QWP's is AlGaAs/GaAs, where the material of the Quantum well is GaAs and the barrier material is AlGaAs, where the fraction of aluminum in THz QWP's is typically in the range from 0.8% to 5.4% (H. C. Liu, Song, SpringThorpe, & Cao, 2004)). In general, QWIP can be divided in to two types, namely: photoconductive and photovoltaic, where most of the models that have been introduced for THz QWPs are photoconductive QWIPs. The main difference between the two types of QWIP is that photoconductive QWIPs works in the presence of external voltage bias, while photovoltaic detectors work at zero bias. According to the type of doping there is the n-type QWIP and the p-type QWIP, but because of the lack of a good performance for the p-type QWIPs, most of the investigated QWIPs models are n-doped. However, n-type QWIPs can't absorb incident radiation with polarization perpendicular to the Quantum Well growth direction because of the selection rule of intersubband transition (Cao & Liu, 2011). Hence, different light-coupling methods are used in n-type QWIP to improve the device responsivity, such as metal-grating couplers for normal incident radiation (R. Zhang et al., 2017). An incidence angle of 45° can also be realized by using a 45° tilted facet coupling, as shown in Figure (1.5).

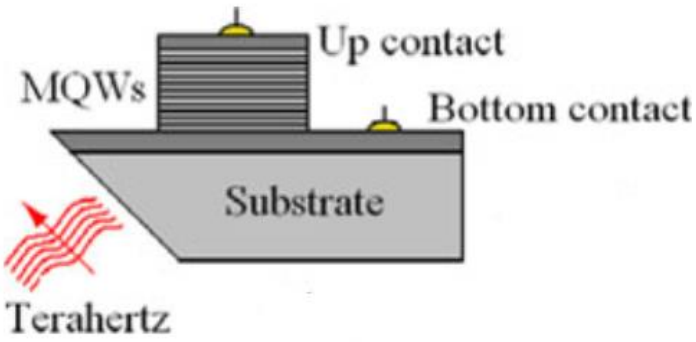

Figure 1.5. *A THz QWP with* 45° *facet coupler* (*Zhou, Li, & Li, 2013*)

2. INTERSUBBAND TRANSITIONS AND FIGURES OF MERIT OF THZ QWPS

2.1. An overview of the problem

A The problem of the potential well is a standard problem in quantum mechanics that usually used to illustrate the quantum properties, such as the discreteness of energy levels that can be occupied by the quantum mechanical system and the wavefunction of a particle such as an electron. The problem has two versions, namely the finite and the infinite quantum well, and solutions to both versions of the problem can be found in almost every introductory-level quantum mechanics textbook (Liboff, 2003; Shankar, 1994).

Generally, when tackling the quantum potential well problem, we aim to solve the Schrödinger equation for the system and find the Eigenstates (wave functions) and Eigenvalues (Energy states). Furthermore, it's desired to study the effect of changing the well's parameters such as the width and height (in the case of finite well) on the behavior of the system. Thus, solving and understanding the different aspects of this problem is crucial for many fields in physics, since the quantum well proved to have many technical applications especially in the fields of electronics and optoelectronics where many devices operate by exploiting the idea of confining charge carriers in a quantum well, devices such as: quantum well infrared photodetectors, superlattice optical-devices, high electron mobility transistors, Quantum cascade laser, etc. In practice, the quantum well is represented by a particular kind of Heterostructures in which one thin layer of semiconductor (such as GaAs) is surrounded by two layers of other semiconductors with greater band gaps (e.g AlGaAs) ("Optical properties of quantum wells,"). In this structure, the middle layer forms the well region and the surrounding layers work as the barriers of the well. In the coming sections, we will discuss the cases of infinite and finite quantum well in more depth.

2.2. The infinite quantum well

A one-dimensional infinite quantum well is a system in which a particle is surrounded by impenetrable barriers represented by infinite potential energy extending from the barriers of the well to every point outside the well, while the potential inside the well can be zero or any finite potential.

The problem is usually used in the sense of explaining the difference between the behavior of a particle in a classical system and in a quantum system. For instance, a

particle in a big box is allowed to move at any speed inside the box and its position is not subject to probability. On the other hand, for a particle in a very small box, namely an infinite quantum well, the behavior of such a particle becomes subject to quantum effects, where the particle can only occupy certain energy levels, moreover, a particle in infinite quantum well can never have a zero energy, meaning that the particle is in a constant movement all the time. Furthermore, the position of the particle in the quantum well is probabilistic, meaning that it is more likely to be found at certain positions than at others, the positions at which the particle is most likely to be found are called antinodes, while on the other hand, the particle can never be found at the nodes.

Let's suppose that we have a one-dimensional infinite quantum well with a width of ***a***, where the origin is chosen to be at the middle of the well **(Fig 2.1)**, and the potential of the well is as follows:

$$V(x) = \begin{cases} \infty & x \leq -\frac{a}{2} \\ 0 & |x| < \frac{a}{2} \\ \infty & x \geq \frac{a}{2} \end{cases} \tag{2.1}$$

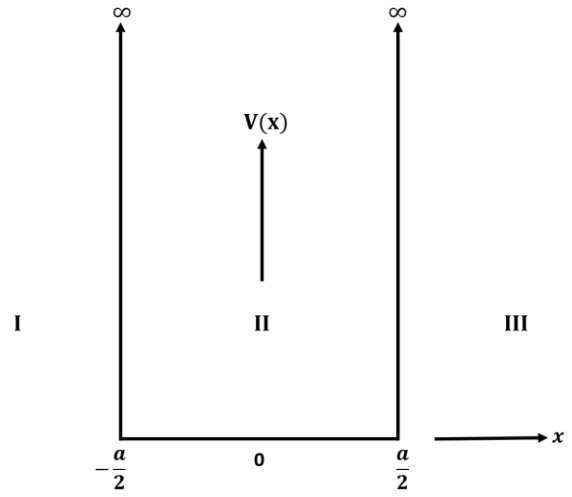

Figure 2.1. *The infinite quantum well in one dimension.*

The system shown in Figure (2.1) is divided into three regions, where regions **I** and **III** have a potential of ∞**,** and the potential in region II is **0.**

Now, our goal is to solve the Schrodinger equation for a particle of mass m trapped in a box (the infinite well). So, The Schrodinger equation for this problem is

$$-\frac{\hbar^2}{2m}\frac{d^2\psi(x)}{dx^2}+V(x)\psi(x)=E\psi(x) \tag{2.2}$$

Rearranging this equation gives us the following

$$\frac{d^2\psi(x)}{dx^2}+\frac{2m}{\hbar^2}[E-V(x)]\psi(x)=0 \tag{2.3}$$

This is an ordinary differential equation and its solution depends on the value of $V(x)$. Hence, the solutions for each case of $V(x)$ are as follows:

❖ Regions I and III where $V(x)=\infty$

Since the potential at the walls of the well is infinite, then it's impossible for the particle inside the well to penetrate the wall and exist in regions I and III, in terms of wavefunction, we can say that the wavefunction is zero in regions I and III. To get this solution analytically, we will solve the Schrodinger equation for a potential V, then we will substitute with $(V=\infty)$ to get the value of $\psi(x)$ in regions I and III

$$\frac{d^2\psi(x)}{dx^2}-\frac{2m}{\hbar^2}[V-E]\psi(x)=0$$

We can set the coefficient of $\psi(x)$ to k^2, so the equation becomes

$$\frac{d^2\psi(x)}{dx^2}-k^2\psi(x)=0 \tag{2.4}$$

Where $V>E$, and k is described by the following equation

$$k=\sqrt{\frac{2m}{\hbar^2}[V-E]} \tag{2.5}$$

the solution to the differential equation above is

$$\psi(x) = Ae^{-kx} + Be^{kx} \tag{2.6}$$

A and B are two arbitrary coefficients, however, we need to set $B = 0$ because the term e^{kx} blows up to infinity when $x \to \infty$, and this doesn't satisfy the requirements of the wavefunction. Hence, out wavefunctions becomes

$$\psi(x) = Ae^{-kx} \tag{2.7}$$

Now, we need to set $V = \infty$ in equation (2.5) and substitute the value of k into equation (2.7) to get the wavefunction in regions **I** and **III**

$$k = \sqrt{\frac{2m}{\hbar^2}[\infty - E]} = \infty$$

Hence, the wavefunction in regions I and III is

$$\psi(x) = Ae^{-\infty} = 0$$

Thus

$$\psi_I(x) = \psi_{III}(x) = 0 \tag{2.8}$$

- Regions II where $V(x) = 0$

In this case, the Schrodinger equation is written as follows

$$\frac{d^2\psi(x)}{dx^2} + \frac{2mE}{\hbar^2}\,\psi(x) = 0 \tag{2.9}$$

which can be written as follows

$$\frac{d^2\psi(x)}{dx^2} + k\,\psi(x) = 0 \tag{2.10}$$

Where k is

$$k = \sqrt{\frac{2mE}{\hbar^2}} \tag{2.11}$$

The solution of equation (2.10) is

$$\psi_{II}(x) = Ae^{ikx} + Be^{-ikx} \tag{2.12}$$

A and *B* are arbitrary coefficients that can be determined by applying the boundary conditions at the walls of the well, where the wavefunction must be continues at these positions, which demands the satisfaction of the following two conditions

$$\psi_I\left(-\frac{a}{2}\right) = \psi_{II}\left(-\frac{a}{2}\right) = 0 \tag{2.13}$$

and

$$\psi_{II}\left(\frac{a}{2}\right) = \psi_{III}\left(\frac{a}{2}\right) = 0 \tag{2.14}$$

Substituting from equation (2.12) into equations (2.13) and (2.14) results in the following

$$Ae^{-\frac{ika}{2}} + Be^{\frac{ika}{2}} = 0 \tag{2.15}$$

$$Ae^{\frac{ika}{2}} + Be^{-\frac{ika}{2}} = 0 \tag{2.16}$$

this system of equations can be written in the matrix form, as shown below

$$\begin{bmatrix} e^{-\frac{ika}{2}} & e^{\frac{ika}{2}} \\ e^{\frac{ika}{2}} & e^{-\frac{ika}{2}} \end{bmatrix} \begin{bmatrix} A \\ B \end{bmatrix} = \begin{bmatrix} 0 \\ 0 \end{bmatrix}$$

This secular equation has a nontrivial solution only when the determinant of the first matrix is zero [21], which can be written as follows:

$$e^{-ika} - e^{ika} = 0 \tag{2.17}$$

But we know that $\sin(x)$ can be written as

$$\sin(x) = \frac{e^{ix} - e^{-ix}}{2i}$$

Applying this to equation (2.17), we get the following

$$-2i\ sin(ka) = 0 \tag{2.18}$$

By using the periodicity of the $\sin(x)$ function, we conclude that equation (2.18) is only true when

$$k = \frac{n\pi}{a}, \qquad n = 0, \pm 1, \pm 2, \pm 3, \ldots \tag{2.19}$$

In order to find the wavefunction, we need to substitute from (2.19) into (2.15) or (2.16) and solve to find one of the coefficients in terms of the other, as shown bellow

$$Ae^{-\frac{in\pi}{2}} + Be^{\frac{in\pi}{2}} = 0$$

by dividing both sides of the equation by $\frac{e^{-in\pi}}{2}$, we get the following

$$A = -e^{in\pi}B \tag{2.20}$$

but we know that $e^{i\pi} = -1$, so $e^{in\pi} = (-1)^n$. Hence, equation (2.20) can be written as

$$A = -(-1)^n B$$

substituting this result into equation (2.12) gives us two different wavefunctions, one for even values of n and the other is for the odd values of n

$$\psi_n(x) = -(-1)^n Be^{ikx} + Be^{-ikx}$$

- When n is odd

$$\psi_n(x) = B\left(e^{ikx} + e^{-ikx}\right)$$

multiplying and dividing the right-hand side of the equation by 2, and using the fact that $\cos(x) = \frac{e^{ix}+e^{-ix}}{2}$,we can write the following

$$\psi_n(x) = 2Bcos(kx)$$

$$\psi_n(x) = 2Bcos\left(\frac{n\pi}{a}x\right) \tag{2.21}$$

The constant B in equation (2.21) is a normalization constant to be found by applying the normalization condition of the wavefunction, as follows

$$\int_{-\infty}^{\infty} \psi(x) \times \psi^*(x) dx = 1$$

The integration limits for our wavefunction are $-\frac{a}{2}$ and $\frac{a}{2}$, so we can write the following

$$4B^2 \int_{-\frac{a}{2}}^{\frac{a}{2}} \cos^2\left(\frac{n\pi}{a}x\right) dx = 1$$

Using the trigonometric relation $\cos^2(x) = \frac{1+\cos(2x)}{2}$, we find that the integral above evaluates to

$$2B^2 a = 1$$

$$B = \sqrt{\frac{1}{2a}}$$

Substituting for B into equation (2.21) gives us the following

$$\psi_n(x) = \sqrt{\frac{2}{a}}\, cos\left(\frac{n\pi}{a}x\right), \quad n \text{ odd} \tag{2.22}$$

And when n is even, we have

$$\psi_n(x) = -B\left(e^{ikx} - e^{-ikx}\right)$$

Multiplying and dividing the right-hand side of the equation by $2i$, and using the fact that $\sin(x) = \frac{e^{ix} - e^{-ix}}{2i}$,we can write the following

$$\psi_n(x) = -2iBsin(kx) \tag{2.23}$$

By applying the normalization condition on the wavefunction in equation (2.23), we find that the constant $B = i\sqrt{\frac{1}{2a}}$, and by substituting for B into equation (2.23) we get the following result for the wavefunction

$$\psi_n(x) = \sqrt{\frac{2}{a}}\, sin\left(\frac{n\pi}{a}x\right), \;\; n \text{ even} \tag{2.24}$$

Now that we found the eigenstates (wavefunctions), we need to find the eigenvalues, which can be done by substituting for k with its value from equation (2.19) into equation (2.11), then rearranging the result to isolate E. Notice that E will be depending on the quantum number n, so we write E_n

$$k^2 = \frac{2mE}{\hbar^2}$$

$$\frac{n^2\pi^2}{a^2} = \frac{2mE_n}{\hbar^2}$$

Hence, the eigenvalues of the system can be written as

$$E_n = \frac{n^2\hbar^2\pi^2}{2ma^2} \tag{2.25}$$

Next, I will be using the results in equations (2.22), (2.24) and (2.25) to write a program in Python that shows the wavefunctions and the eigenvalues of an electron trapped in an infinite quantum well.

The first three wavefunctions and their corresponding probability functions of an electron trapped in an infinite quantum well with a width of 40 A^o are shown in figures (2.2) and (2.3), respectively.

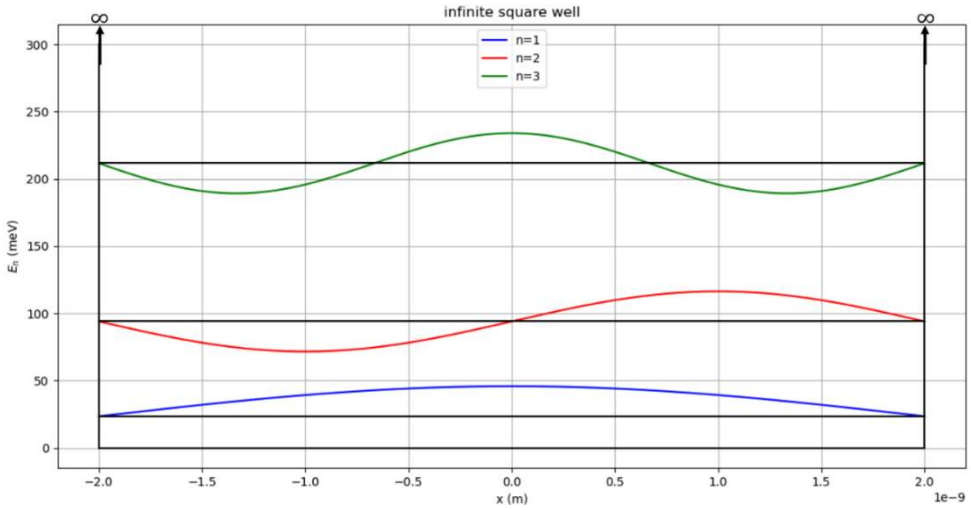

Figure 2.2. *The wave functions of the first three states.*

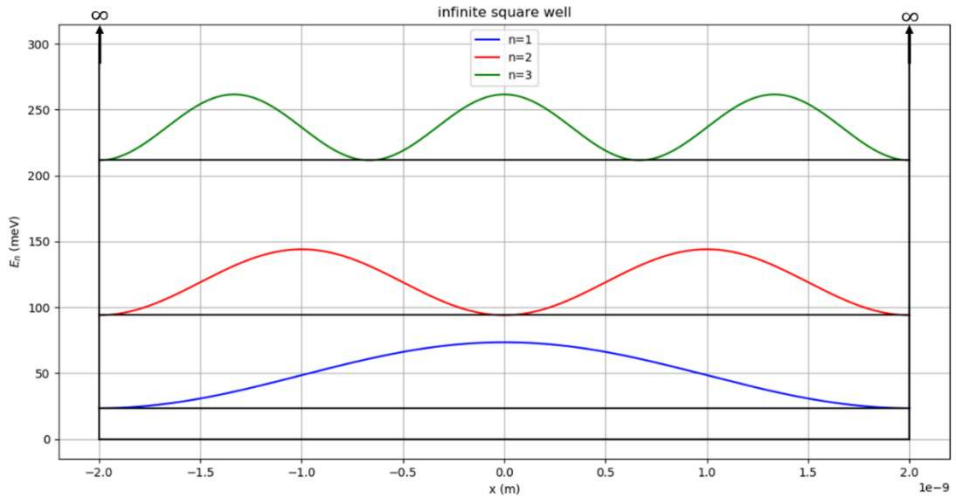

Figure 2.3. *The probability functions of the first three states.*

2.3. The finite square quantum well

Another important version of the quantum potential well problem, is the finite quantum well, in which the walls of the well have a finite height, namely, a finite potential. The potential describing such a system can be written as follows

$$V(x) = \begin{cases} V_1 & x \leq -\frac{a}{2} \\ 0 & |x| < \frac{a}{2} \\ V_2 & x \geq \frac{a}{2} \end{cases} \tag{2.26}$$

For the sake of generality, this problem will be solved for a finite quantum well with a different potential on each side of the well, meaning that $V_1 \neq V_2$.

The system we wish to solve the Schrodinger equation for is shown in figure (2.4). As done with the infinite quantum well, the aim here is to solve the Schrodinger equation and find the eigenvectors and the eigenvalues of a particle trapped inside the well.

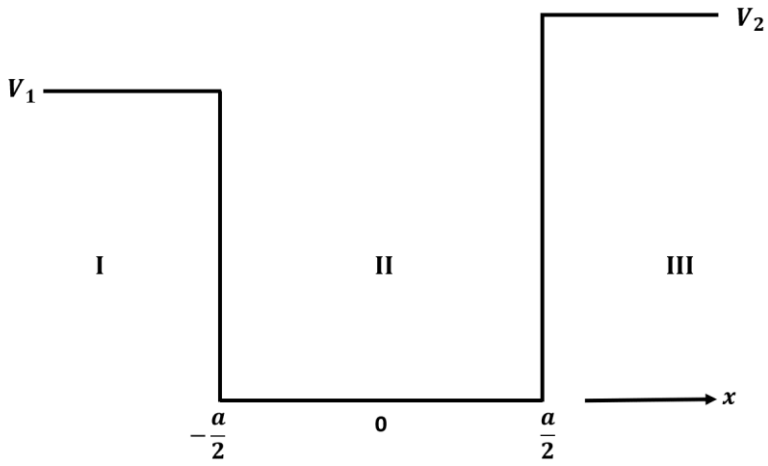

Figure 2.4. *Finite quantum well with a width of a.*

The time independent Schrodinger equation for the system is shown in equation (2.3). By substituting with the appropriate value of $V(x)$ from equation (2.26) into equation (2.3), we get three differential equations, one for each potential, and the solutions to these ODEs are as follows

$$\psi_I(x) = Ce^{k_1 x} + Fe^{-k_1 x} \tag{2.27}$$

$$\psi_{II}(x) = Asin(kx) + Bcos(kx) \tag{2.28}$$

$$\psi_{III}(x) = Ee^{k_2 x} + De^{-k_2 x} \tag{2.29}$$

However, we notice that we need to set $F = E = 0$, since the terms $e^{-k_1 x}$ and $e^{k_2 x}$ blow up to infinity when $x \to -\infty$ and $x \to \infty$ respectively, which doesn't satisfy the requirements of the wavefunction as it has to vanish at $x \to -\infty$ and $x \to \infty$. Hence, the wavefunctions becomes

$$\psi_I(x) = Ce^{k_1 x} \tag{2.30}$$

$$\psi_{II}(x) = Asin(kx) + Bcos(kx) \tag{2.31}$$

$$\psi_{III}(x) = De^{-k_2 x} \tag{2.32}$$

where k, k_1 and k_2 are described as follows

$$k = \sqrt{\frac{2mE}{\hbar^2}} \tag{2.33}$$

$$k_1 = \sqrt{\frac{2m(V_1 - E)}{\hbar^2}} \tag{2.34}$$

$$k_2 = \sqrt{\frac{2m(V_2 - E)}{\hbar^2}} \tag{2.35}$$

Where $E < V$ in all cases, and the constants A, B, C and D are arbitrary coefficients that can be found after applying the boundary conditions and using the normalization conditions.

The boundary conditions we demand here are that the wavefunction and it's first derivative be continuous at the walls of the well, which can be written as follows

$$\psi_I\left(-\frac{a}{2}\right) = \psi_{II}\left(-\frac{a}{2}\right)$$

$$\frac{d\psi_I\left(-\frac{a}{2}\right)}{dx} = \frac{d\psi_{II}\left(-\frac{a}{2}\right)}{dx}$$

$$\psi_{II}\left(\frac{a}{2}\right) = \psi_{III}\left(\frac{a}{2}\right)$$

$$\frac{d\psi_{II}\left(\frac{a}{2}\right)}{dx} = \frac{d\psi_{III}\left(\frac{a}{2}\right)}{dx}$$

By substituting into the last four equations for the wavefunctions from equations (2.30), (2.31) and (2.32), we get the following

$$Ce^{\frac{-k_1 a}{2}} = -Asin\left(\frac{ka}{2}\right) + Bcos\left(\frac{ka}{2}\right) \tag{2.36}$$

$$k_1 Ce^{\frac{-k_1 a}{2}} = kAcos\left(\frac{ka}{2}\right) + kBsin\left(\frac{ka}{2}\right) \tag{2.37}$$

$$Asin\left(\frac{ka}{2}\right) + Bcos\left(\frac{ka}{2}\right) = De^{-\frac{k_2 a}{2}} \tag{2.38}$$

$$kAcos\left(\frac{ka}{2}\right) - kBsin\left(\frac{ka}{2}\right) = -k_2 De^{-\frac{k_2 a}{2}} \tag{2.39}$$

Equations (2.36), (2.37), (2.38) and (2.39) can be written in the matrix form as follows:

$$\begin{bmatrix} -sin\left(\frac{ka}{2}\right) & cos\left(\frac{ka}{2}\right) & -e^{\frac{-k_1 a}{2}} & 0 \\ kcos\left(\frac{ka}{2}\right) & ksin\left(\frac{ka}{2}\right) & -k_1 e^{\frac{-k_1 a}{2}} & 0 \\ sin\left(\frac{ka}{2}\right) & cos\left(\frac{ka}{2}\right) & 0 & -e^{-\frac{k_2 a}{2}} \\ kcos\left(\frac{ka}{2}\right) & -ksin\left(\frac{ka}{2}\right) & 0 & k_2 e^{-\frac{k_2 a}{2}} \end{bmatrix} \begin{bmatrix} A \\ B \\ C \\ D \end{bmatrix} = \begin{bmatrix} 0 \\ 0 \\ 0 \\ 0 \end{bmatrix} \tag{2.40}$$

In order for the system of equations shown in (2.40) to have a nontrivial solution, the determinant of the coefficients matrix must vanish, and we can use this idea to find the eigenvalues numerically. The idea is to plot the determinant as a function of E, where k, k_1 and k_2 are all functions in E. In the plot of the determinant versus the energy E, we look for the points at which the determinant intersects with the E axis, namely the points at which the determinant is zero, and the energies corresponding to these points are our eigenvalues.

A Mathematica program has been developed to solve this problem for and electron trapped in a finite quantum well with a width of 100 A^{o} and represented by the following potential

$$V(x) = \begin{cases} 0.6 \text{ eV} & x \leq -\frac{a}{2} \\ 0 & |x| < \frac{a}{2} \\ 0.8 \text{ eV} & x \geq \frac{a}{2} \end{cases} \tag{2.41}$$

The program finds the first three eigenvalues of the system and plots the wavefunction for each state. It also finds the normalization constants A, B, C and D. To find the normalization constants, we write equations (2.36) and (2.37) together in the matrix form, and do the same for equations (2.38) and (2.39), as follows:

$$\begin{bmatrix} e^{\frac{-k_1 a}{2}} & 0 \\ 0 & k_1 e^{\frac{-k_1 a}{2}} \end{bmatrix} \begin{bmatrix} C \\ C \end{bmatrix} = \begin{bmatrix} -sin\left(\frac{ka}{2}\right) & cos\left(\frac{ka}{2}\right) \\ kcos\left(\frac{ka}{2}\right) & ksin\left(\frac{ka}{2}\right) \end{bmatrix} \begin{bmatrix} A \\ B \end{bmatrix} \tag{2.42}$$

$$\begin{bmatrix} e^{\frac{-k_2 a}{2}} & 0 \\ 0 & -k_2 e^{\frac{-k_2 a}{2}} \end{bmatrix} \begin{bmatrix} D \\ D \end{bmatrix} = \begin{bmatrix} sin\left(\frac{ka}{2}\right) & cos\left(\frac{ka}{2}\right) \\ kcos\left(\frac{ka}{2}\right) & -ksin\left(\frac{ka}{2}\right) \end{bmatrix} \begin{bmatrix} A \\ B \end{bmatrix} \tag{2.43}$$

Next, we do some algebraic manipulation to isolate the matrix that contains A and B in both equations (2.42) and (2.43), and we do that by multiplying both sides from the left by the inverse of the coefficient matrix on the right.

Hence, equations (2.42) and (2.43) becomes

$$\frac{1}{-k} \begin{bmatrix} ksin\left(\frac{ka}{2}\right) & -cos\left(\frac{ka}{2}\right) \\ -kcos\left(\frac{ka}{2}\right) & -sin\left(\frac{ka}{2}\right) \end{bmatrix} \begin{bmatrix} e^{\frac{-k_1 a}{2}} & 0 \\ 0 & k_1 e^{\frac{-k_1 a}{2}} \end{bmatrix} \begin{bmatrix} C \\ C \end{bmatrix} = \begin{bmatrix} A \\ B \end{bmatrix}$$

$$\begin{bmatrix} -sin\left(\frac{ka}{2}\right) e^{\frac{-k_1 a}{2}} & \frac{k_1}{k} cos\left(\frac{ka}{2}\right) e^{\frac{-k_1 a}{2}} \\ cos\left(\frac{ka}{2}\right) e^{\frac{-k_1 a}{2}} & \frac{k_1}{k} sin\left(\frac{ka}{2}\right) e^{\frac{-k_1 a}{2}} \end{bmatrix} \begin{bmatrix} C \\ C \end{bmatrix} = \begin{bmatrix} A \\ B \end{bmatrix} \tag{2.44}$$

applying the same thing for equation (2.43), we get the following

$$\begin{bmatrix} sin\left(\frac{ka}{2}\right) e^{\frac{-k_2 a}{2}} & \frac{-k_2}{k} cos\left(\frac{ka}{2}\right) e^{\frac{-k_2 a}{2}} \\ cos\left(\frac{ka}{2}\right) e^{\frac{-k_2 a}{2}} & \frac{k_2}{k} sin\left(\frac{ka}{2}\right) e^{\frac{-k_2 a}{2}} \end{bmatrix} \begin{bmatrix} D \\ D \end{bmatrix} = \begin{bmatrix} A \\ B \end{bmatrix} \tag{2.45}$$

To simplify the calculations, we name the coefficients matrices on the left sides of equations (2.44) and (2.45) matrix Z and matrix L, such that

$$Z = \begin{bmatrix} -sin\left(\frac{ka}{2}\right)e^{\frac{-k_1 a}{2}} & \frac{k_1}{k}cos\left(\frac{ka}{2}\right)e^{\frac{-k_1 a}{2}} \\ cos\left(\frac{ka}{2}\right)e^{\frac{-k_1 a}{2}} & \frac{k_1}{k}sin\left(\frac{ka}{2}\right)e^{\frac{-k_1 a}{2}} \end{bmatrix} \tag{2.46}$$

$$L = \begin{bmatrix} sin\left(\frac{ka}{2}\right)e^{\frac{-k_2 a}{2}} & \frac{-k_2}{k}cos\left(\frac{ka}{2}\right)e^{\frac{-k_2 a}{2}} \\ cos\left(\frac{ka}{2}\right)e^{\frac{-k_2 a}{2}} & \frac{k_2}{k}sin\left(\frac{ka}{2}\right)e^{\frac{-k_2 a}{2}} \end{bmatrix} \tag{2.47}$$

The plan now is to make use of the fact that the right sides of equations (2.44) and (2.45) are the same, which allows us to write the following

$$\begin{bmatrix} Z_{11} & Z_{12} \\ Z_{21} & Z_{22} \end{bmatrix} \begin{bmatrix} C \\ C \end{bmatrix} = \begin{bmatrix} L_{11} & L_{12} \\ L_{21} & L_{22} \end{bmatrix} \begin{bmatrix} D \\ D \end{bmatrix} \tag{2.48}$$

the equation above gives us the chance to write the constant D in terms of C, as follows

$$L_{11}D + L_{12}D = Z_{11}C + Z_{12}C$$

$$D = \frac{Z_{11} + Z_{12}}{L_{11} + L_{12}}C \tag{2.49}$$

by using equation (2.44), we can find A and B in terms of C as well, as shown bellow

$$\begin{bmatrix} Z_{11} & Z_{12} \\ Z_{21} & Z_{22} \end{bmatrix} \begin{bmatrix} C \\ C \end{bmatrix} = \begin{bmatrix} A \\ B \end{bmatrix}$$

$$A = Z_{11}C + Z_{12}C \tag{2.50}$$

$$B = Z_{21}C + Z_{22}C \tag{2.51}$$

Finally, we can use the normalization condition to find the value of C, then by substituting into equation (2.49), (2.50) and (2.51), we can find the other constants. Where the normalization condition is as follows

$$\int_{-\infty}^{-\frac{a}{2}} |\psi_I(x)|^2 dx + \int_{-\frac{a}{2}}^{\frac{a}{2}} |\psi_{II}(x)|^2 dx + \int_{\frac{a}{2}}^{\infty} |\psi_{III}(x)|^2 dx = 1 \tag{2.52}$$

Mathematica has been used to evaluate this integral numerically and determined the value of C, which then was used to find the other normalization constants and getting the normalized wavefunctions as well.

The energies of the first three states was found to be as shown in table (2.1).

Table 2.1. *The energies of the first three states of the system mentioned earlier in this section.*

E_1	0.0400 eV
E_2	0.1586 eV
E_3	0.3491 eV

Figure (2.5) shows the wavefunctions of the first three states, where the y-axis represents the energy in (meV).

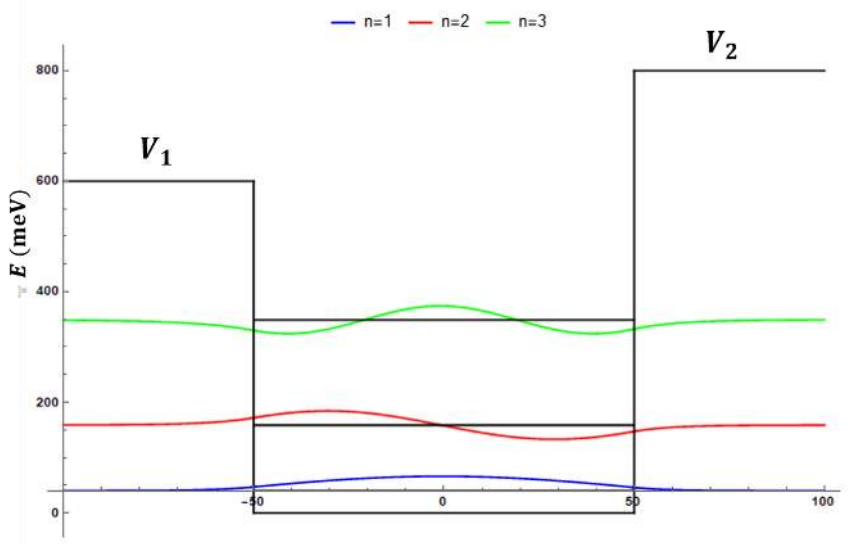

Figure 2.5. *The wavefunctions of the electron in the first three states.*

Next, the same program has been used to plot the probability density functions of the first three states, as shown in figure (2.6). Figures (2.7), (2.8) and (2.9) show the behavior of the first three eigenvalues as the potential V_1 increases, and it's found that these energies increase as V_1 increase.

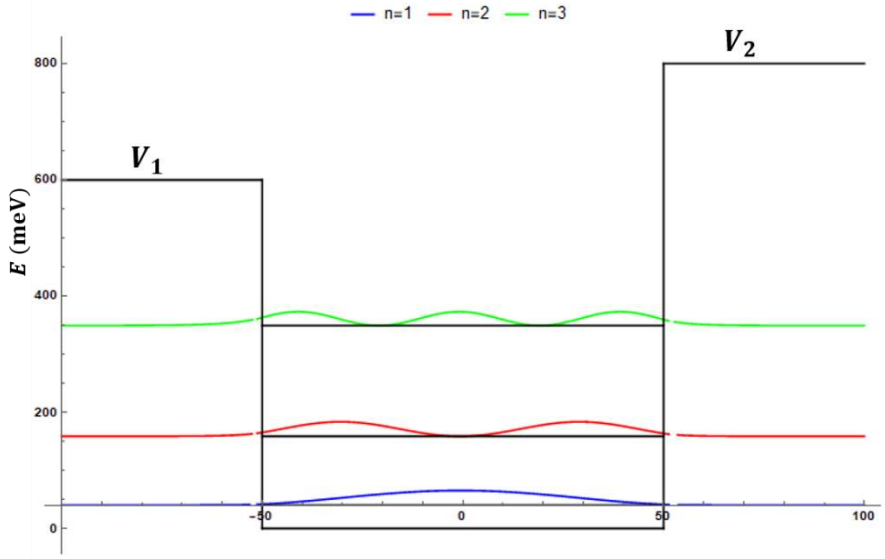

Figure 2.6. *The plot the probability density functions of the first three states.*

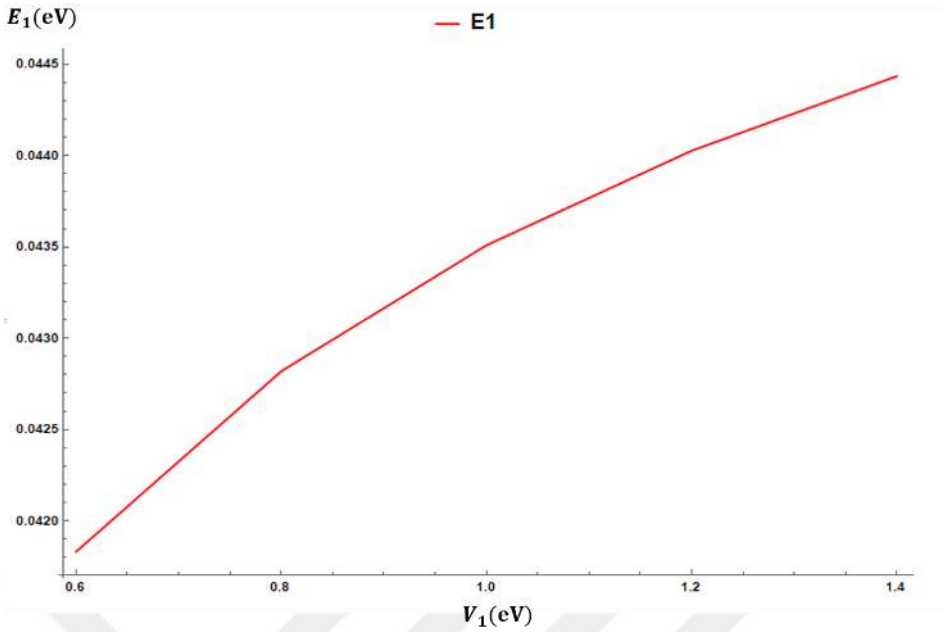

Figure 2.7. *The graph of E_1 versus V_1.*

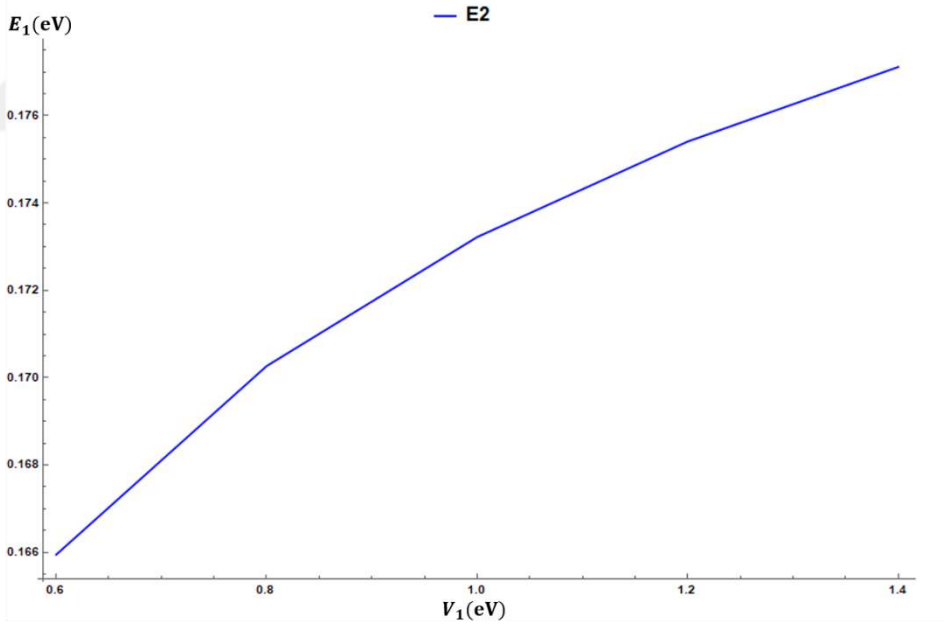

Figure 2.8. *The graph of E_2 versus V_1.*

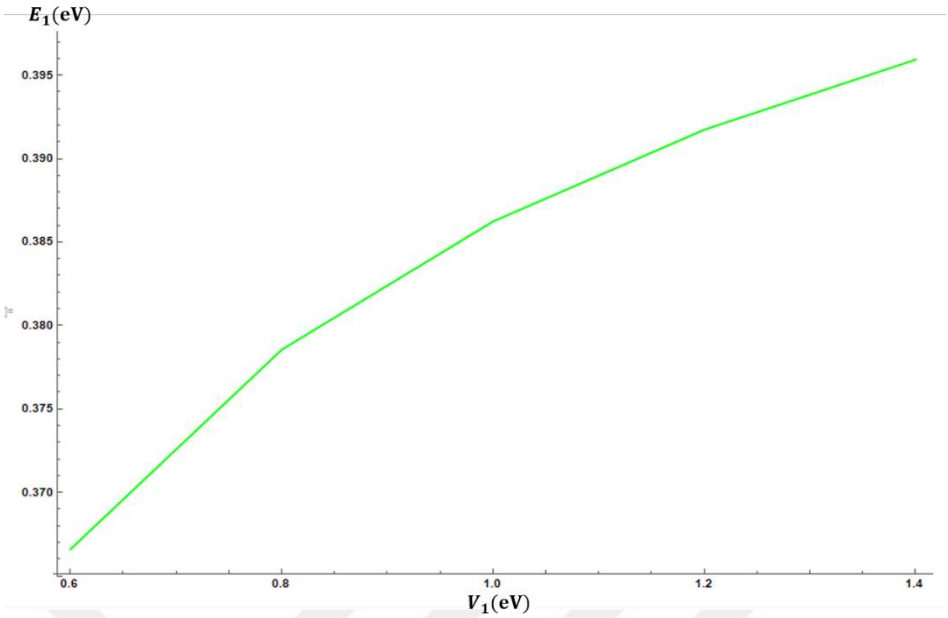

Figure 2.9. *The graph of E_3 versus V_1.*

It is also useful to illustrate the relation between the width of the well and the energy of each state, 8 different widths, starting with 100 A^o and ending by a width of 170 A^o, with a step of 10 A^o have been used for this purpose. The results shown that the energy decreases as the width of the well increases, which can be seen from Figure (2.10)

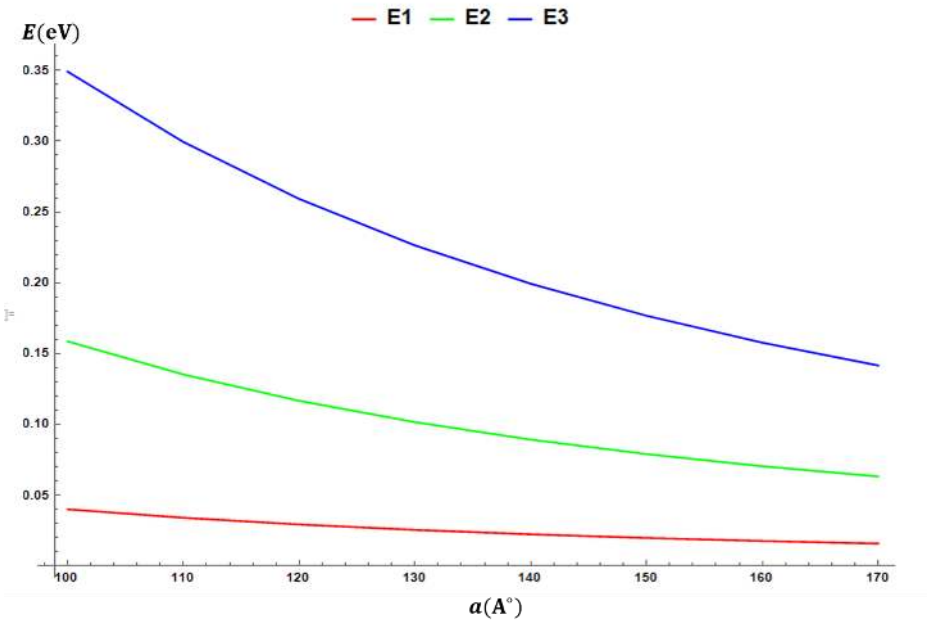

Figure 2.10. *The graph different well widths versus the first three eigenvalues.*

The problem of finite quantum well is very important and has many applications in different topics in physics and that is because it can be used very efficiently to model a variety of real systems, such as: QWIPs, quantum cascade laser, etc.

The problem is usually solved numerically because when we try to find the eigenvalues of the system, we get a transcendental equation, which can't be solved analytically. So, in this section I introduced the method I used to solve the finite square potential quantum well problem, and it is an important step in building up towards the main topic of the thesis, which will be significantly depending on making use of the finite quantum well as a model for the system of study, namely the THz Quantum Well Photodetector.

2.4. The Quantum Well in the presence of Electric Field

We mentioned in the previous section that the quantum well can be used to model many physical systems in optoelectronics and other fields in physics and engineering. In practice, quantum wells are constructed due to the difference in the band gaps between different materials, which cause offsets in the conduction and the valence bands of the neighboring materials. When solving the quantum well problem, the energy subbands of the quantum well are one of the most important parameters that contributes to the optical and electrical behaviors of the system, and those levels has been found to experience drastic shifts when Electric field is applied to the well (Boltaev, Loiko, Rzaev, & Sibeldin, 2000). In this section, I will be numerically solving the problem of finite quantum well in the presence of electric field, to find the first and second energy levels and their corresponding wavefunctions for an electron trapped in the quantum well of choice.

First, we write the Schrodinger equation for the system while including the potential energy due to the presence of an Electric field, as follows

$$-\frac{\hbar^2}{2m}\frac{d^2\psi(x)}{dx^2} + [V(x) + qFx]\psi(x) = E\psi(x) \tag{2.53}$$

Where F is the electric field strength and q is the electron's charge. Rearranging equation (2.53), we get the following

$$-\frac{\hbar^2}{2m}\frac{d^2\psi(x)}{dx^2}+[V(x)+qFx-E]\psi(x)=0 \tag{2.54}$$

reducing the unites of the system will make our calculations more convenient, as it will decrease the number of factors we need to deal with (Enderlein, Holz, & Gondar, 1989). Hence, we will be using the ground state energy of the infinite quantum well to reduce the units of the potential V and the energy E, where ground state energy of an infinite quantum well with a width of L can be obtained from equation (2.25) by replacing a with L and setting $n=1$, ass follows

$$E_o=\frac{\hbar^2\pi^2}{2mL^2} \tag{2.55}$$

Where E_o is the ground state energy of the infinite quantum well. Now, before proceeding to write down the reduced unites, the well I will be solving the Schrodinger equation for is shown in figure (2.11) and it has the following potential:

$$V(x)=\begin{cases} V_o & x\le 0 \\ 0 & 0<x<L \\ V_o & x\ge L \end{cases} \tag{2.56}$$

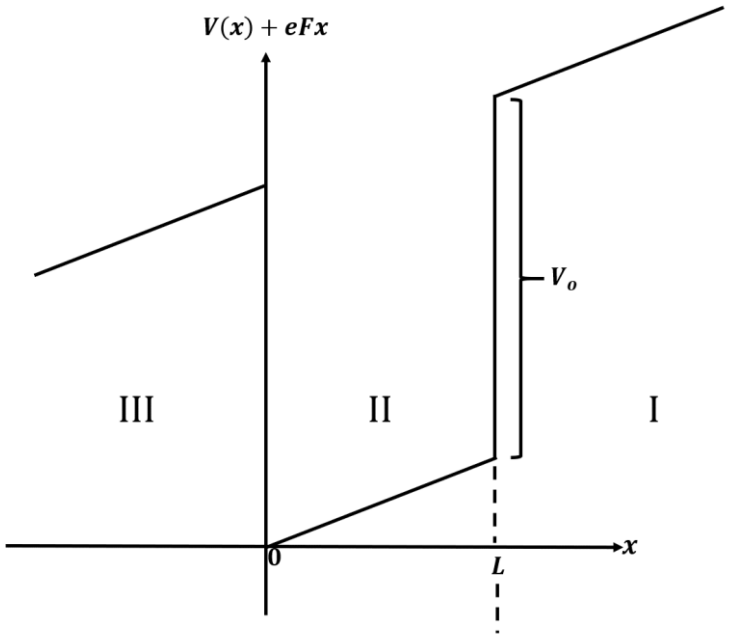

Figure 2.11. *A finite quantum well in the presence of Electric field.*

Actually, V_o has been chosen to be equal to the conduction band offset between **GaAs** and $\mathbf{Al_{0.35}Ga_{0.65}As}$**.** Hence, we have two versions of equation (2.54), one for the region II, and one for regions I and III. However, I will write the general version of the Schrodinger with the reduced units, then I will replace the potential with the appropriate value for each region.

The reduced units for the energy and the potential are as follows:

$$\tilde{E} = E/E_o \tag{2.57}$$

$$\frac{V(x)}{E_o} = \begin{cases} V_{oo} & \text{regions I and III} \\ 0 & \text{region II} \end{cases} \tag{2.58}$$

Likewise, we also need to get the reduced unite for the electric field and to use a spatial coordinate that is normalized to the width of the well, and we do that by dividing x by L to get the following:

$$\tilde{x} = \frac{x}{L} \tag{2.59}$$

and the reduced unit for the electric field is

$$\tilde{F} = \frac{qFL}{E_o} \tag{2.60}$$

deriving both sides in equation (2.59) twice, gives us the following

$$\frac{d^2}{dx^2} = \frac{1}{L^2}\frac{d^2}{d\tilde{x}^2} \tag{2.61}$$

after applying some algebraic manipulation to equation (2.54) and substituting from equations (2.57), (2.59), (2.60) and (2.61), we get the following differential equation

$$\frac{d^2\psi(\tilde{x})}{d\tilde{x}^2} - \pi^2\left[\frac{V(x)}{E_o} + \tilde{F}\tilde{x} - \tilde{E}\right]\psi(\tilde{x}) = 0 \tag{2.62}$$

now, it's the time to substitute for the potentials from equation (2.58) into equation (2.62) to get two different equation, as follows

$$\frac{d^2\psi(\tilde{x})}{d\tilde{x}^2} - \pi^2[V_{00} + \tilde{F}\tilde{x} - \tilde{E}]\psi(\tilde{x}) = 0, \qquad \text{Regions I and III} \tag{2.63}$$

$$\frac{d^2\psi(\tilde{x})}{d\tilde{x}^2} - \pi^2[\tilde{F}\tilde{x} - \tilde{E}]\psi(\tilde{x}) = 0, \qquad \text{Regions II} \tag{2.64}$$

Let's interduce two new parameters with aim of reducing the numbers of factors in equations (2.63) and (2.64), the new variables are u_1 and u_2, and they are described as follows

$$u_1 = A\pi^2[V_{00} + \tilde{F}\tilde{x} - \tilde{E}] \tag{2.65}$$

$$u_2 = B\pi^2[\tilde{F}\tilde{x} - \tilde{E}] \tag{2.66}$$

Where A and B are constants to be found in the following calculations. Deriving both sides in equations (2.65) and (2.66) twice, gives us the following

$$\frac{d^2}{d\tilde{x}^2} = A^2\pi^4\tilde{F}^2\frac{d^2}{du_1^2} \tag{2.67}$$

$$\frac{d^2}{d\tilde{x}^2} = B^2\pi^4\tilde{F}^2\frac{d^2}{du_2^2} \tag{2.68}$$

Substituting from equations (2.65) and (2.67) into equation (2.63) results in the following equations

$$A^2\pi^4\tilde{F}^2\frac{d^2\psi}{du_1^2} - \frac{u_1}{A}\psi = 0, \qquad \text{Regions I and III} \tag{2.69}$$

Rearranging equation (2.69) yields the following relation

$$A^3\pi^4\tilde{F}^2\frac{d^2\psi}{du_1^2} - u_1\psi = 0, \qquad \text{Regions I and III} \tag{2.70}$$

We would like to find A that will make the term $A^3\pi^4\tilde{F}^2$ equal to unity. Hence, we write the following

$$A = \frac{1}{\left(\pi^2\tilde{F}\right)^{\frac{2}{3}}} \tag{2.71}$$

Hence, equation (w.70) becomes

$$\frac{d^2\psi}{du_1^2} - u_1\psi = 0, \qquad \text{Regions I and III} \tag{2.72}$$

where u_1 is described as follows

$$u_1(\tilde{x}) = \left(\frac{\pi}{\tilde{F}}\right)^{\frac{2}{3}}(\tilde{F}\,\tilde{x} + V_{oo} - \tilde{E}) \tag{2.73}$$

By substituting from equation (2.66) and (2.68) into equation (2.64) and following the same procedures we followed with u_1, we get the following for u_2

$$A = \frac{1}{\left(\pi^2\tilde{F}\right)^{\frac{2}{3}}} \tag{2.74}$$

$$\frac{d^2\psi}{du_2^2} - u_2\psi = 0, \qquad \text{Region II} \tag{2.75}$$

$$u_2(\tilde{x}) = \left(\frac{\pi}{\tilde{F}}\right)^{\frac{2}{3}} (\tilde{F}\,\tilde{x} - \tilde{E}) \tag{2.76}$$

The solutions to equations (2.72) and (2.75) are Airy function of the first and second kind, so the solutions to these equations represent the wavefunctions in the three different regions, namely I, II and III.

$$\psi(\tilde{x}) = \begin{cases} a_1 Ai(u_1) + b_1 Bi(u_1) & \text{I} \\ a_2 Ai(u_2) + b_2 Bi(u_2) & \text{II} \\ a_3 Ai(u_1) + b_3\, Bi(u_1) & \text{III} \end{cases} \tag{2.77}$$

Notice that the wavefunction is written as a function of $\tilde{x}$, and that is true because u_1 and u_2 are both functions of $\tilde{x}$.

It is convenient to take a look at the graphs of both functions, which are given in figures (2.12) and (2.13)

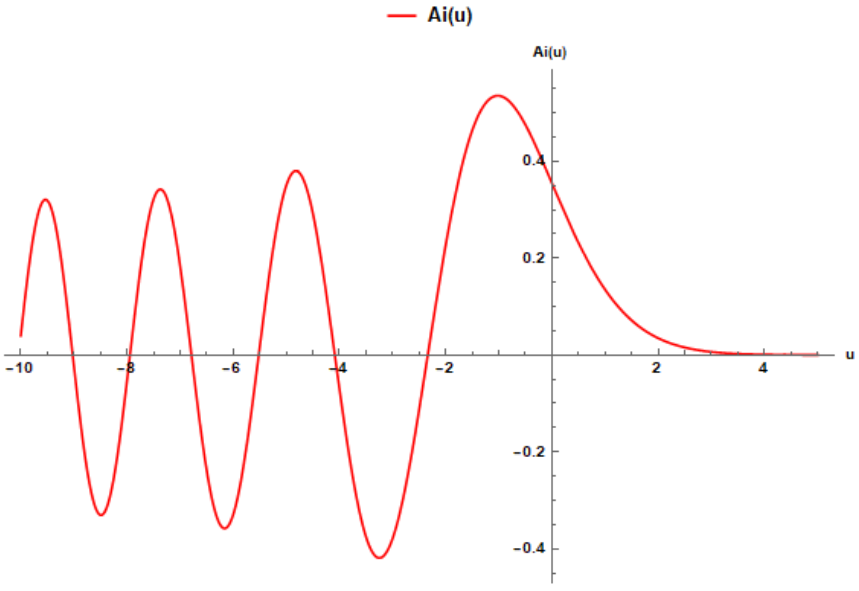

Figure 2.12. *The graph of Airy function of the first kind.*

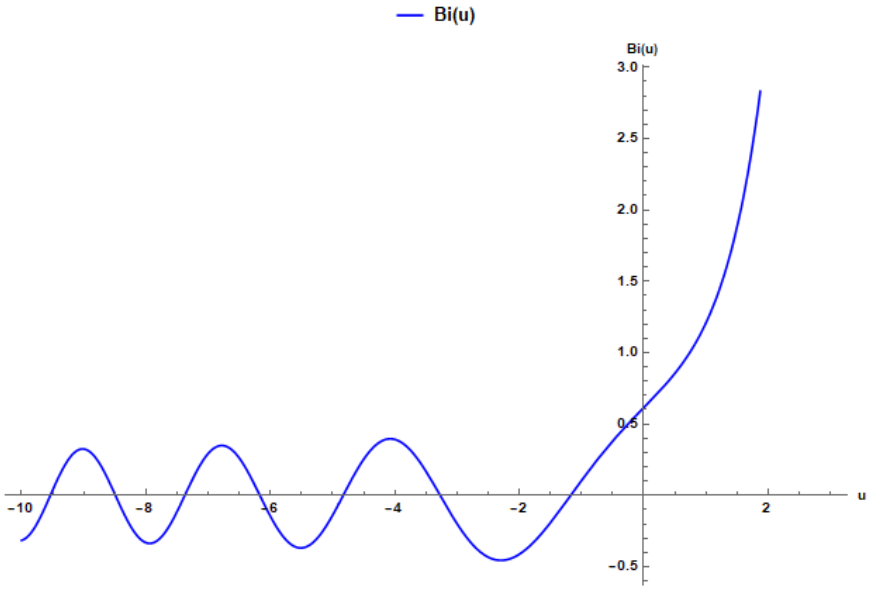

Figure 2.13. *The graph of Airy function of the second kind.*

We know that the wavefunction $\psi(x)$ must be zero as $x \to \infty$, however, it is obvious from Figure (2.11) that $\boldsymbol{Bi(u)}$ blows up to infinity for positive values of u, which means that we need to set $b_1 = 0$ and keep only $\boldsymbol{Ai(u)}$ as the wavefunction on the right side of the well (region I).

On the other hand, we can see from Figures (2.12) and (2.13) that both $\boldsymbol{Ai(u)}$ and $\boldsymbol{Bi(u)}$ have an acceptable behavior as a wavefunction for negative values of u, however, we know that one of the boundary conditions that must be satisfied by the wavefunction of a finite quantum well is that both the wavefunction and its first derivative must be continuous at the boundaries. And if we look at the graph of $Ai(u) + Bi(u)$ in figure (2.14), we find that it's plausible to assume that the solution in region **III** can be written in terms of Airy function of the second kind only, meaning that we need to set $a_3 = 0$. The reasoning behind this step is that $Bi(u)$ starts decaying right from the boundaries, which allows its derivative to match the derivative of $Ai(u) + Bi(u)$, while $Ai(u)$ can't stand as a solution by itself because its derivative at the left wall of the well can never equal the derivative of $Ai(u) + Bi(u)$.

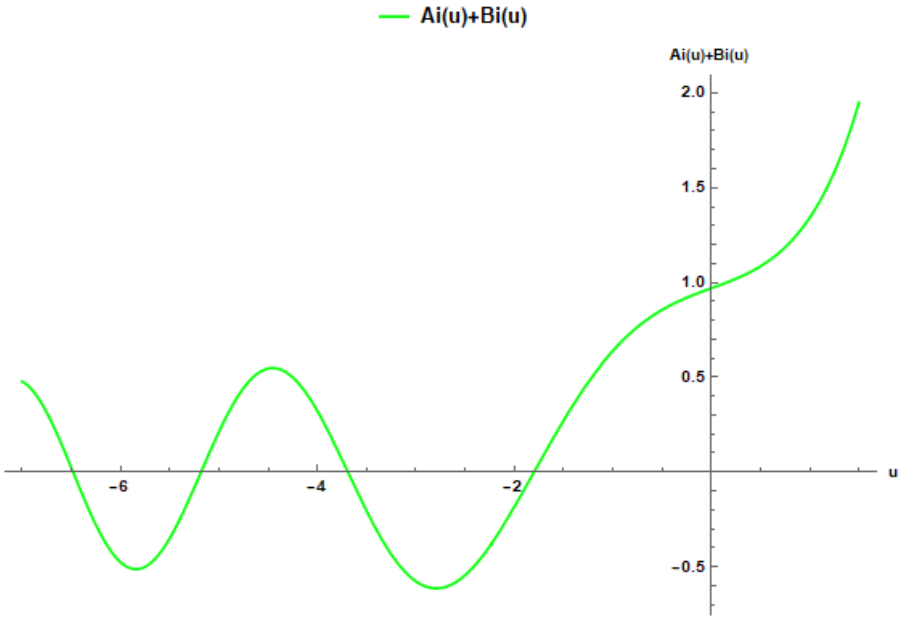

Figure 2.14. *The graph of* $Ai(u) + Bi(u)$.

By comparing figures (2.11) and (2.12), we find that after multiplying the two graphed functions with some constant, they can satisfy the conditions of continuity at the left side boundary of the well.

Taking all the aforementioned points into account, equation (2.77) becomes

$$\psi(\tilde{x}) = \begin{cases} a_1 Ai(u_1) & \text{I} \\ a_2 Ai(u_2) + b_2 Bi(u_2) & \text{II} \\ b_3\, Bi(u_1) & \text{III} \end{cases} \tag{2.78}$$

Now it is about time we apply the boundary conditions, and since our spatial coordinates are normalized to the width of the well, then we demand that the wave function and its first derivative be continuous at $\tilde{x} = 1$ and $\tilde{x} = 0$.

$$\psi_I\big(u_1(1)\big) = \psi_{II}(u_2(1)) \tag{2.79}$$

$$\frac{d\psi_I\big(u_1(1)\big)}{d\tilde{x}} = \frac{d\psi_{II}\big(u_2(1)\big)}{d\tilde{x}} \tag{2.80}$$

$$\psi_{II}\big(u_2(0)\big) = \psi_{III}(u_1(0)) \tag{2.81}$$

$$\frac{d\psi_{II}\big(u_2(0)\big)}{d\tilde{x}} = \frac{d\psi_{III}\big(u_1(0)\big)}{d\tilde{x}} \tag{2.82}$$

By substituting from equation (2.78) into equations (2.79), (2.80), (2.81) and (2.82), we get the following

$$a_1 \mathrm{Ai}(u_1(1)) = a_2 \mathrm{Ai}\big(u_2(1)\big) + b_2 \mathrm{Bi}(u_2(1)) \tag{2.83}$$

$$a_1 \frac{d\mathrm{Ai}\big(u_1(1)\big)}{d\tilde{x}} = a_2 \frac{dAi\big(u_2(1)\big)}{d\tilde{x}} + b_2 \frac{d\mathrm{Bi}\big(u_2(1)\big)}{d\tilde{x}} \tag{2.84}$$

$$a_2 \mathrm{Ai}\big(u_2(0)\big) + b_2 \mathrm{Bi}\big(u_2(0)\big) = b_3 \mathrm{Bi}(u_1(0)) \tag{2.85}$$

$$a_2 \frac{d\mathrm{Ai}\big(u_2(0)\big)}{d\tilde{x}} + b_2 \frac{d\mathrm{Bi}\big(u_2(0)\big)}{d\tilde{x}} = b_3 \frac{d\mathrm{Bi}\big(u_1(0)\big)}{d\tilde{x}} \tag{2.86}$$

The last four equations can be written in the matrix form to give us the following system

$$\begin{bmatrix} \mathrm{Ai}(u_1(1)) & -\mathrm{Ai}(u_2(1)) & -\mathrm{Bi}(u_2(1)) & 0 \\ \mathrm{Ai}'(u_1(1)) & -\mathrm{Ai}'(u_2(1)) & -\mathrm{Bi}'(u_2(1)) & 0 \\ 0 & \mathrm{Ai}(u_2(0)) & \mathrm{Bi}(u_2(0)) & -\mathrm{Bi}(u_1(0)) \\ 0 & \mathrm{Ai}'(u_2(0)) & \mathrm{Bi}'(u_2(0)) & -\mathrm{Bi}'(u_1(0)) \end{bmatrix} \begin{bmatrix} a_1 \\ a_2 \\ b_2 \\ b_3 \end{bmatrix} = \begin{bmatrix} 0 \\ 0 \\ 0 \\ 0 \end{bmatrix} \tag{2.87}$$

Where Ai' is the first derivative of the Airy function of the first kind and Bi' is the first derivative of the Airy function of the second kind. Now, the system of equation shown in (2.87) have a nontrivial solution only when the determinant of the coefficient matrix equals zero. The determinant will be a function in the energy E since both u_1 and u_2 are functions in $\tilde{E}$ and we know that $\tilde{E} = E/E_o$, so the idea is to draw the determinant versus the energy E, and the eigenvalues we are looking for will be at the points at which the determinant intersects with the Energy axis.

The constants a_1, a_2, b_2 and b_3 also need to be determined using the normalization condition and the equations we got as a result for applying the boundary conditions. But first we need to find three of the constants in terms of the fourth constant, and we do that by writing equations (2.83) and (2.84) together in the matrix form, then we do the same for equations (2.85) and (2.86), after that we algebraically manipulate the two systems of equations to get the results we want.

$$\begin{bmatrix} \mathrm{Ai}(u_1(1)) & 0 \\ 0 & \mathrm{Ai}'(u_1(1)) \end{bmatrix} \begin{bmatrix} a_1 \\ a_1 \end{bmatrix} = \begin{bmatrix} \mathrm{Ai}(u_2(1)) & \mathrm{Bi}(u_2(1)) \\ \mathrm{Ai}'(u_2(1)) & \mathrm{Bi}'(u_2(1)) \end{bmatrix} \begin{bmatrix} a_2 \\ b_2 \end{bmatrix} \tag{2.88}$$

$$\begin{bmatrix} \mathrm{Bi}(u_1(0)) & 0 \\ 0 & \mathrm{Bi}'(u_1(0)) \end{bmatrix} \begin{bmatrix} b_3 \\ b_3 \end{bmatrix} = \begin{bmatrix} \mathrm{Ai}(u_2(0)) & \mathrm{Bi}(u_2(0)) \\ \mathrm{Ai}'(u_2(0)) & \mathrm{Bi}'(u_2(0)) \end{bmatrix} \begin{bmatrix} a_2 \\ b_2 \end{bmatrix} \tag{2.89}$$

Let

$$\mathrm{L} = \begin{bmatrix} \mathrm{Ai}(u_2(1)) & \mathrm{Bi}(u_2(1)) \\ \mathrm{Ai}'(u_2(1)) & \mathrm{Bi}'(u_2(1)) \end{bmatrix} \tag{2.90}$$

and

$$S = \begin{bmatrix} \mathrm{Ai}(u_2(0)) & \mathrm{Bi}(u_2(0)) \\ \mathrm{Ai}'(u_2(0)) & \mathrm{Bi}'(u_2(0)) \end{bmatrix} \tag{2.91}$$

Using the fact that $\mathrm{Ai(x)Bi'(x)} - \mathrm{Ai'(x)Bi(x)} = \pi^{-1}$, we multiply both sides of equation (2.88) from the left by $\mathrm{L}^{-1} = \pi^{-1}$, and multiply both sides of equation (2.89) by $\mathrm{S}^{-1} = \pi^{-1}$ to get the following

$$\pi^{-1} \begin{bmatrix} \mathrm{Ai}(u_1(1)) & 0 \\ 0 & \mathrm{Ai}'(u_1(1)) \end{bmatrix} \begin{bmatrix} a_1 \\ a_1 \end{bmatrix} = \begin{bmatrix} a_2 \\ b_2 \end{bmatrix} \tag{2.92}$$

$$\pi^{-1}\begin{bmatrix}\mathrm{Bi}(u_1(0)) & 0\\ 0 & \mathrm{Bi}'(u_1(0))\end{bmatrix}\begin{bmatrix}b_3\\ b_3\end{bmatrix}=\begin{bmatrix}a_2\\ b_2\end{bmatrix} \tag{2.93}$$

to simplify our notation, we can write the following

$$\mathrm{LL}=\pi^{-1}\begin{bmatrix}\mathrm{Ai}(u_1(1)) & 0\\ 0 & \mathrm{Ai}'(u_1(1))\end{bmatrix} \tag{2.94}$$

$$SS=\pi^{-1}\begin{bmatrix}\mathrm{Bi}(u_1(0)) & 0\\ 0 & \mathrm{Bi}'(u_1(0))\end{bmatrix} \tag{2.95}$$

Using equation (2.92) together with equation (2.94) allows us to write the following

$$a_2=LL_{11}a_1 \tag{2.96}$$

$$b_2=LL_{22}\,a_1 \tag{2.97}$$

similarly, by using equation (2.93) together with (2.95), we get

$$a_2=SS_{11}b_3 \tag{2.98}$$

substituting from equation (2.96) into (2.98) results in

$$b_3 = \frac{LL_{11}}{SS_{11}} a_1 \tag{2.99}$$

Finally, a Mathematica program has been written based on the methods mentioned in this chapter, and calculated the first two eigenvalues for a finite quantum well with a width of 60 A^o and have a depth of $V_o = 0.289$ eV, the calculations were done in the presence of an electric field of a strength of 4.8×10^4 V/cm.The energies of the first two states are listed in table (2.2)

Table 2.2. *The energies of the first two states of the quantum well in the presence of electric field.*

E_1	0.084 eV
E_2	0.256 eV

The wavefunctions of the first two states are shown in Figure (2.15), where the y-axis represents the potential energy in (eV), and the horizontal axis represents the reduced spatial coordinate, namely $\tilde{x}$. The probability densities of the same states are shown in Figure (2.16).

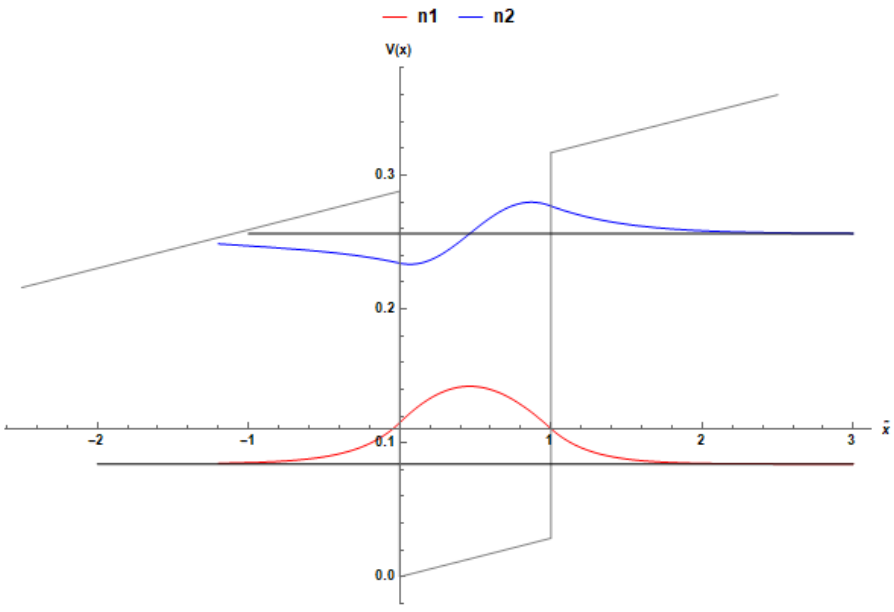

Figure 2.15. *The wavefunctions of the first two states of the system discussed in this section.*

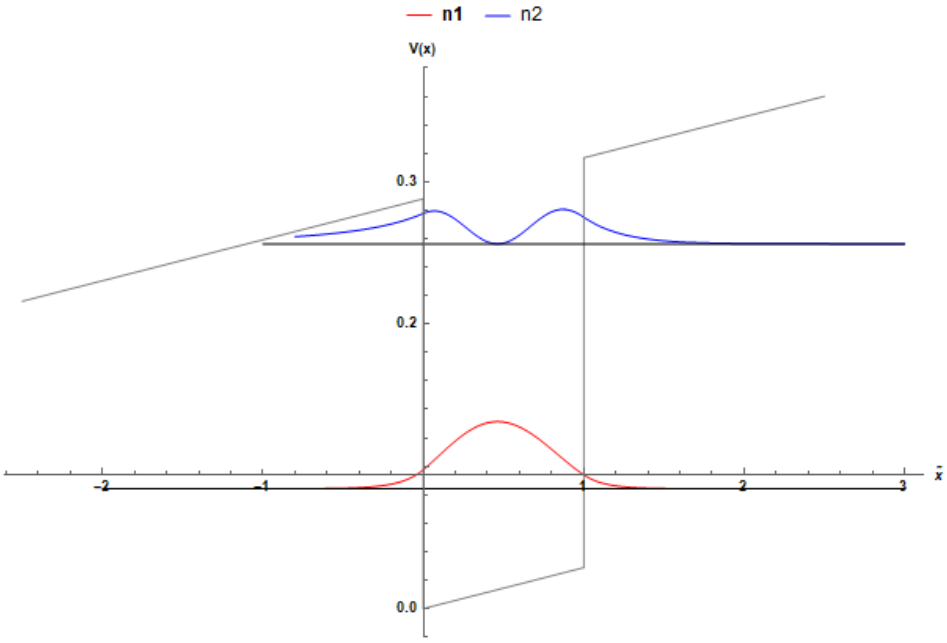

Figure 2.16. *The probability densities of the first two states.*

3. INTERSUBBAND TRANSITIONS AND FIGURES OF MERIT OF THZ QWPS

3.1. Theory of Intersubband Transitions in QWIP

Most of QWIPs are based on the intersubband transitions that take place in the conduction band, and the most used material system for designing these devices is $Al_xGa_{1-x}As/GaAs$, which is the material that will be used to design the THz QWP in this thesis. So, it is convenient to talk about the rate of transition rate between the subbands of the quantum well, which is governed by Fermi's golden rule. Electrons confined in the ground state of the quantum well experience transition to a state of higher energy when the system is subjected to external perturbation, and the source of perturbation in the case of optical intersubband transitions is the incident electromagnetic radiation on the active region of the device (Okhovat-Alavian, Afzali-Kusha, & Kamarei, 2001). Using Fermi's golden rule, the intersubband transitions rate between the ith and the fth states can be written as follows

$$W = \frac{2\pi}{\hbar}\left|\langle\psi_f|H_{int}|\psi_i\rangle\right|^2\delta(E_f - E_i - \hbar\omega) \tag{3.1}$$

where W is the rate of transition between the states i and f, E_i and E_f are the energies of the initial and the final state respectively, H_{int} is the electron-photon interaction Hamiltonian and ω is the angular frequency of the photons. Next step, is to workout the interaction Hamiltonian, which can be written as follows

$$H_{int} = -\frac{e}{2m}(\mathbf{A}\cdot\mathbf{p} + \mathbf{p}\cdot\mathbf{A}) \tag{3.2}$$

where $\boldsymbol{A}$ is the vector potential. By using the Coulomb gauge $\boldsymbol{\nabla}\cdot\mathbf{A} = \mathbf{0}$ and the fact that $\mathbf{p} = -i\hbar\nabla$, we can say that $\mathbf{A}\cdot\mathbf{p} = \mathbf{p}\cdot\mathbf{A}$, which means that equation (3.2) becomes

$$H_{int} = -\frac{e}{m}\mathbf{A}\cdot\mathbf{p} \tag{3.3}$$

Now, the vector potential has the following form

$$\mathbf{A} = \frac{A_o}{2}\hat{e}\left(e^{i\boldsymbol{q}\cdot\boldsymbol{r}}e^{-i\omega t} + e^{-i\boldsymbol{q}\cdot\boldsymbol{r}}e^{i\omega t}\right) \tag{3.4}$$

where $A_o = \left(\frac{2\hbar\phi}{\epsilon_0 n_r \omega c}\right)^{1/2}$, $\hat{e}$ is a unit vector in the direction of the polarization (which the direction of the electric field), q is the wave vector of the electromagnetic wave and ω is the angular frequency of the incident photons. However, the second term of equation (3.4) is related to the emission of photons when electrons go to a lower state of energy, and we are interested in the first term of (3.4) which is related to the absorption process of photons (Chuang, 2009; Ridley, 2013). Hence, we ignore the second term and substitute equation (3.4) into (3.3) to get the interaction Hamiltonian for the absorption process, which writes as follows

$$H_{int} = -\frac{e}{2m}\left(\frac{2\hbar\phi}{\epsilon_0 n_r \omega c}\right)^{1/2} e^{i\boldsymbol{q}\cdot\boldsymbol{r}}\hat{e}\cdot\mathbf{p}\, e^{-i\omega t}$$

$$H_{int} = -\frac{e}{m}\left(\frac{\hbar\phi}{2\epsilon_0 n_r \omega c}\right)^{1/2} e^{i\boldsymbol{q}\cdot\boldsymbol{r}}\hat{e}\cdot\mathbf{p}\, e^{-i\omega t} \tag{3.5}$$

m is the effective mass of the electron in the quantum well, ϕ is the impinging photons flux, n_r is the refractive index of the material, c is the speed of light and $\mathbf{p}$ is the momentum vector of the electron. The goal is to find the rate of transition from state i to state f, and to do this, equation (3.5) must be substituted into equation (3.1), however, in order to find the matrix element $\langle\psi_f|H_{int}|\psi_i\rangle$, the wavefunction ψ must be defined first. Another point that worth mentioning is that the term $e^{-i\omega t}$ is considered to be absorbed in the delta function of equation (3.1) when we substitute the expression of H_{int} into (3.1), so the time dependence will be dropped when we find the matrix element $\langle\psi_f|H_{int}|\psi_i\rangle$ (Ridley, 2013). Since the quantization of the states is in the growth direction of the quantum well (z −direction) and the electron is free to move in the $x-y$ plane, then the wavefunction can be written as a multiplication of two wavefunctions, namely a function in z (ψ_z) and a planewave in the $x-y$ plane (ψ_{xy}). Hence

$$\psi = \psi_z\psi_{xy} = \frac{1}{\sqrt{S}}e^{i\boldsymbol{k}_{xy}\cdot\boldsymbol{r}_{xy}}\psi_z \tag{3.6}$$

Where S is the in-plane area on which the electromagnetic radiation is incident, and $\boldsymbol{k}_{xy}$ is the two-dimensional wavevector in the $x-y$ plane. Now we can write the matrix element $\langle\psi_f|H_{int}|\psi_i\rangle$ as follows

$$\langle\psi_f|H_{int}|\psi_i\rangle = -\frac{e}{m}\sqrt{\frac{\hbar\phi}{2\epsilon_0 n_r\omega c}}\,\frac{1}{S}\left\langle e^{i\boldsymbol{k}_{xy,f}\cdot\boldsymbol{r}_{xy}}\psi_{z,f}\middle|e^{i\boldsymbol{q}\cdot\boldsymbol{r}}\hat{e}\cdot\mathbf{p}\middle|e^{i\boldsymbol{k}_{xy,i}\cdot\boldsymbol{r}_{xy}}\psi_{z,i}\right\rangle$$

For the sake of simplicity, I am going to write the term $-\frac{e}{m}\sqrt{\frac{\hbar\phi}{2\epsilon_0 n_r\omega c}}$ as a constant C. Using the relations $\mathbf{p} = \mathbf{p_{xy}} + \mathbf{p_z}$ and $e^{i\boldsymbol{q}\cdot\boldsymbol{r}} = e^{i(\boldsymbol{q}_{xy}+\boldsymbol{q}_z)\cdot(\boldsymbol{r}_{xy}+\boldsymbol{r}_z)}$, the previous equation becomes

$$\langle\psi_f|H_{int}|\psi_i\rangle = \mathrm{C}\times\frac{1}{S}\left\langle e^{i\mathbf{k}_{xy,f}\cdot\mathbf{r}_{xy}}\psi_{z,f}\left|e^{i(\mathbf{q}_{xy}+\mathbf{q}_z)\cdot(\mathbf{r}_{xy}+\mathbf{r}_z)}\hat{e}\cdot(\mathbf{p}_{xy}+\mathbf{p}_z)\right|e^{i\mathbf{k}_{xy,i}\cdot\mathbf{r}_{xy}}\psi_{z,i}\right\rangle$$

$$= \mathrm{C}\times\frac{1}{S}\left\langle e^{i\mathbf{k}_{xy,f}\cdot\mathbf{r}_{xy}}\psi_{z,f}\left|e^{i(\mathbf{q}_{xy}+\mathbf{q}_z)\cdot(\mathbf{r}_{xy}+\mathbf{r}_z)}\hat{e}\cdot\mathbf{p}_{xy}\right|e^{i\mathbf{k}_{xy,i}\cdot\mathbf{r}_{xy}}\psi_{z,i}\right\rangle$$

$$+\mathrm{C}\times\frac{1}{S}\left\langle e^{i\mathbf{k}_{xy,f}\cdot\mathbf{r}_{xy}}\psi_{z,f}\left|e^{i(\mathbf{q}_{xy}+\mathbf{q}_z)\cdot(\mathbf{r}_{xy}+\mathbf{r}_z)}\hat{e}\cdot\mathbf{p}_z\right|e^{i\mathbf{k}_{xy,i}\cdot\mathbf{r}_{xy}}\psi_{z,i}\right\rangle$$

$$= \mathrm{C}\times\frac{1}{S}\left\langle e^{i\mathbf{k}_{xy,f}\cdot\mathbf{r}_{xy}}\psi_{z,f}\left|e^{i\mathbf{q}_{xy}\cdot\mathbf{r}_{xy}}\,e^{i\mathbf{q}_z\cdot\mathbf{r}_z}\,\hat{e}\cdot\mathbf{p}_{xy}\right|e^{i\mathbf{k}_{xy,i}\cdot\mathbf{r}_{xy}}\psi_{z,i}\right\rangle$$

$$+\mathrm{C}\times\frac{1}{S}\left\langle e^{i\mathbf{k}_{xy,f}\cdot\mathbf{r}_{xy}}\psi_{z,f}\left|e^{i\mathbf{q}_{xy}\cdot\mathbf{r}_{xy}}\,e^{i\mathbf{q}_z\cdot\mathbf{r}_z}\,\hat{e}\cdot\mathbf{p}_z\right|e^{i\mathbf{k}_{xy,i}\cdot\mathbf{r}_{xy}}\psi_{z,i}\right\rangle$$

Hence, the matrix element becomes

$$\begin{aligned}\langle\psi_f|H_{int}|\psi_i\rangle = \frac{\mathrm{C}}{S}&\left\langle e^{i\mathbf{k}_{xy,f}\cdot\mathbf{r}_{xy}}\left|e^{i\mathbf{q}_{xy}\cdot\mathbf{r}_{xy}}\;\hat{e}\right.\right.\\&\left.\cdot\mathbf{p}_{xy}\left|e^{i\mathbf{k}_{xy,i}\cdot\mathbf{r}_{xy}}\right\rangle\langle\psi_{z,f}\left|e^{i\mathbf{q}_z\cdot\mathbf{r}_z}\right|\psi_{z,i}\right\rangle\\&+\frac{\mathrm{C}}{S}\left\langle e^{i\mathbf{k}_{xy,f}\cdot\mathbf{r}_{xy}}\left|e^{i\mathbf{q}_{xy}\cdot\mathbf{r}_{xy}}\;\right.\right.\left|e^{i\mathbf{k}_{xy,i}\cdot\mathbf{r}_{xy}}\right\rangle\langle\psi_{z,f}|\hat{e}\\&\left.\cdot\mathbf{p}_z\,e^{i\mathbf{q}_z\cdot\mathbf{r}_z}\right|\psi_{z,i}\rangle\end{aligned}\tag{3.7}$$

The first in equation (3.7) vanishes because photons cannot cause direct transitions between free carriers [11]. by inserting the term $\frac{1}{S}$ in the bra-kets, equation (3.7) becomes

$$\langle\psi_f|H_{int}|\psi_i\rangle = \mathrm{C}\int dxdy\; e^{-i\mathbf{k}_{xy,f}\cdot\mathbf{r}_{xy}}\,e^{i\mathbf{q}_{xy}\cdot\mathbf{r}_{xy}}\,e^{i\mathbf{k}_{xy,i}\cdot\mathbf{r}_{xy}}\,\langle\psi_{z,f}|\hat{e}\cdot\mathbf{p}_z\,e^{i\mathbf{q}_z\cdot\mathbf{r}_z}|\psi_{z,i}\rangle$$

$$= \mathrm{C}\int dxdy\; e^{-i\mathbf{k}_{xy,f}\cdot\mathbf{r}_{xy}}\,e^{i(\mathbf{k}_{xy,i}+\mathbf{q}_{xy})\cdot\mathbf{r}_{xy}}\,\langle\psi_{z,f}|\hat{e}\cdot\mathbf{p}_z\,e^{i\mathbf{q}_z\cdot\mathbf{r}_z}|\psi_{z,i}\rangle$$

The first integral can be written as a delta function and the vector $\mathbf{p_z}$ equals $p_z\hat{z}$ where p_z is the magnitude of $\mathbf{p_z}$. Hence, the last equation can be written as follows:

$$\langle \psi_f | H_{int} | \psi_i \rangle = \mathrm{C}\delta_{\boldsymbol{k}_{xy,f},\boldsymbol{k}_{xy,i}+\boldsymbol{q}_{xy}} \, (\hat{e} \cdot \hat{z}) \langle \psi_{z,f} | p_z \, e^{i\boldsymbol{q}_z \cdot \boldsymbol{r}_z} | \psi_{z,i} \rangle \tag{3.8}$$

Using the fact that $\mathbf{q_{xy}}$ is much smaller than $\mathbf{k}_{xy}$ and that $e^{i\boldsymbol{q}_z \cdot \boldsymbol{r}_z} \approx e^{i\boldsymbol{q}_z \cdot \boldsymbol{r}_z} = 1$ because $r_z \ll \lambda$, we can write equation (3.8) as follows

$$\langle \psi_f | H_{int} | \psi_i \rangle = -\frac{e}{m} \sqrt{\frac{\hbar \phi}{2\epsilon_0 n_r \omega c}} \, \delta_{\boldsymbol{k}_{xy,f},\boldsymbol{k}_{xy,i}} \, (\hat{e} \cdot \hat{z}) \langle \psi_{z,f} | p_z | \psi_{z,i} \rangle \tag{3.9}$$

Notice that if the angle between $\hat{e}$ and $\hat{z}$ was $\frac{\pi}{2}$, then the matrix element will vanish to zero and no transition will take place, which the case of incident light with polarization perpendicular to the Quantum Well growth direction. In order to find the total transition rate, we multiply equation (3.1) by the probabilities of occupation of states i and f and sum over i and f. By taking the stimulated emission that causes electrons to move to a lower state of energy into account, the total transition rate can be written as follows

$$\begin{aligned}
W_{\mathrm{tot}} &= \sum_{i,f} W \, f_i(1 - f_f) - \sum_{i,f} W \, f_f(1 - f_i) \\
&= \frac{2\pi}{\hbar} \sum_{i,f} \left| \langle \psi_f | H_{int} | \psi_i \rangle \right|^2 (f_i - f_f) \, \delta(E_f - E_i - \hbar\omega) \\
&= \frac{\pi e^2}{m^2} \frac{\phi}{\epsilon_0 n_r \omega c} (\hat{e} \cdot \hat{z})^2 \times \\
&\sum_{i,f} \left| \langle \psi_{z,f} | p_z | \psi_{z,i} \rangle \right|^2 (\delta_{\boldsymbol{k}_{xy,f},\boldsymbol{k}_{xy,i}})^2 \, (f_i - f_f) \, \delta(E_f - E_i - \hbar\omega)
\end{aligned}$$

for very low temperatures, we assume that $f_f \approx 0$ and $\sum_i f_i = n_{2D} \times S$, where n_{2D} is the 2D electron density in the ground state and S is the in plane area, given that we are dealing with the case of $i = 1$ (the ground state) and $f = 2$ (the first excited state) [Chuang, 2009; (Schneider & Liu, 2007]. Hence, the total transition rate from the ground state to the first excited state is

$$W_{\text{tot}} = \frac{\pi e^2}{m^2}\frac{\phi}{\epsilon_0 n_r \omega c}\sin^2\theta \times \left|\langle\psi_{z,2}|p_z|\psi_{z,1}\rangle\right|^2 \times (n_{2D} \times S)\,\delta(E_2 - E_1 - \hbar\omega) \tag{3.10}$$

$\hat{e}\cdot\hat{z} = \sin\theta$, where θ the angle between of electric field of the incident radiation and the surface of the material, where z is perpendicular to sample surface (growth direction). In the case of intersubband transition, the electric field must have a component in the growth direction in order for the absorption to take place, while in the case of the band to band transition, that is not necessarily the case. It is convenient at this point to introduce the term oscillator strength between the ground state and the first excited state, which is defined as follows

$$f = \frac{2}{m\hbar\omega}\left|\langle\psi_{z,2}|p_z|\psi_{z,1}\rangle\right|^2 \tag{3.11}$$

And can be equivalently written as

$$f = \frac{2m\omega}{\hbar}\left|\langle\psi_{z,2}|z|\psi_{z,1}\rangle\right|^2 \tag{3.12}$$

substituting from (3.11) into (3.10) yields

$$W_{\text{tot}} = \frac{\pi\hbar e^2}{2m}\frac{\phi}{\epsilon_0 n_r c}\sin^2\theta \times f \times (n_{2D} \times S)\,\delta(E_2 - E_1 - \hbar\omega) \tag{3.13}$$

Now we can use the total transition rate obtained in equation (3.13) to determine the absorption quantum efficiency η,which the ratio of the transition rate and the number of photons impinging the well each second.

$$\eta = \frac{W}{\phi S \cos\theta}$$
$$= \frac{\pi \hbar e^2}{2m\epsilon_0 n_r c} \frac{\sin^2\theta}{\cos\theta} f\, n_{2D}\, \delta(E_2 - E_1 - \hbar\omega) \tag{3.14}$$

The lifetime broadening contribution can be included by replacing the delta function in equation (3.14) by Lorentzian lineshape function (H. C. Liu, 1993). So, the absorption quantum efficiency then becomes

$$\eta = \frac{\pi \hbar e^2}{2m\epsilon_0 n_r c} \frac{\sin^2\theta}{\cos\theta} f\, n_{2D} \frac{\Delta E}{\pi(\hbar\omega - E_2 + E_1)^2 + \Delta E^2} \tag{3.15}$$

where ΔE is the half width at half maximum.

3.2. Many-Particle Effects

In the case of QWIPs that works at a frequency larger than the THz range, Many-particle effects do not cause very significant shift in the position of the absorption peak when we include them in the calculations, and one can get a theoretical design in a good a agreement with the experimental results in this case (Helm, 2000). However, the Many-particle effects become so important and have a significant impact on the calculations when it comes to THz QWP, and that is because of the small barrier height and the small energy difference between the subbands. The main effects that need to be considered in the calculations are the exchange-correlation potential, Hartree potential and the depolarization shift (Helm, 2000). First, the Schrodinger equation is solved to determine the energy states, where Schrodinger's equation with Many-particle effects included is written as follows

$$-\frac{\hbar^2}{2m}\nabla^2\psi(r) + [V_{cr}(r) + V_H(r) + V_{xc}(r) + eFz]\psi(r) = E\psi(r) \tag{3.16}$$

V_{cr} is the square well potential due to the difference in the band gaps of the barrier and the well materials, V_H is the Hartree potential which rises up due to the spatial separation of the electrons from the dopants, V_{xc} is the exchange-correlation potential, and the (eFz) is the potential energy due to the external electric field, where F is the electric field strength (Ferré, Razavipour, & Ban, 2013). However, Schrodinger's equation needs to be solved self-consistently with the Poisson equation, where Poisson's equation is used to calculate the Hartree potential, as follows

$$\frac{d^2V_H(z)}{dz^2} = -\frac{e^2}{\varepsilon\varepsilon_0}[n(z) - N_D(z)] \tag{3.17}$$

where e is the electron charge, $N_D(z)$ is the density of ionized dopants, and $n(z)$ is the electrons density. The Hartree potential can be determined by integrating equation (3.17) twice. For a finite temperature, the electron density is given by the following equation

$$n(z) = \sum_i n_i |\psi_i(z)|^2 \tag{3.18}$$

$\psi_i(z)$ is the wave function of ith subband and n_i is the electrons areal density of the same subband (Ozturk, Ergun, Sari, & Sokmen, 2000). The areal density n_i is given by the following relation

$$n_i = \frac{mk_BT}{\pi\hbar^2}\ln\left(1 + e^{\frac{E_f - E_i}{k_BT}}\right) \tag{3.19}$$

where T is the temperature and k_B is Boltzmann constant. Now, we add the Hartree potential and the exchange-correlation potential V_{xc} to the potential of the quantum well in the Schrodinger equation, we solve equation (3.17) self-consistently with the equation (3.16) to find the energy states, where V_{xc} for electrons in a quantum well is written as follows (Graf et al., 2009):

$$V_{xc}(z) = -\left(\frac{9\pi}{4}\right)^{\frac{1}{3}} \times \frac{2}{\pi r_s}\left(1 + \frac{B}{A} r_s \ln\left[1 + \frac{A}{r_s}\right]\right) \times \frac{e^2}{8\pi\varepsilon\varepsilon_0 a^*} \tag{3.20}$$

where $r_s = \left(\frac{4\pi}{3} a^{*3} n(z)\right)^{-\frac{1}{3}}$ is the mean electron distance, $a^* = \frac{\varepsilon}{m} a_B$ is the effective Bohr radius, and $A = 11.4$ and $B = 0.6213$ according to (Graf et al., 2009; Helm, 2000).

The Hartree and exchange-correlation potential account for the static many body effect, and it has been found that there are two main terms that accounts for dynamic many body effects and cause the absorption peak frequency to shift, and these are depolarization shift and the exciton interaction, where the energy at which the absorption takes place is not $E_2 - E_1$, instead its described by the following equation (Helm, 2000):

$$\Delta E'_{21} = \Delta E_{21}\sqrt{1 + \alpha - \beta}$$

Where α accounts for the depolarization shift and β accounts for the excitation shift. α and β are described as follows:

$$\alpha = \frac{2e^2 n_{2D}}{\varepsilon\varepsilon_0 \Delta E_{21}} \int_{-\infty}^{\infty} dz \left[\int_{-\infty}^{z} dz' \psi_2(z')\psi_1(z')\right]^2$$

$$\beta = -\frac{2n_{2D}}{\Delta E_{21}} \int_{-\infty}^{\infty} dz\, \psi_2(z)^2 \psi_1(z)^2 \frac{\partial V_{xc}\big(n(z)\big)}{\partial n(z)}$$

where n_{2D} is the areal carriers density and $n(z)$ is the three-dimensional electron density.

3.3. Photocurrent

When THz photons impinge the electrons confined in the ground state of the quantum well, the electrons get excited and move to the continuum or to the quasi-bound state where they can contribute to the photocurrent under externally applied electric field. When the photocurrent that flows through the conduction band enters an active region,

some of this current gets captured in the quantum well, as shown in Figure (3.1). However, excited electrons in this quantum well will contribute to the total photocurrent with a current called i_{photo}, which is the photocurrent emitted from one quantum well. The previous details can be described by the following equation:

$$I_{photo} = i_{photo} + (1 - p_c)I_{photo} \tag{3.21}$$

Where I_{photo} is the photocurrent in the active region, p_c is the probability of I_{photo} being captured by the quantum well (the capture probability), $p_c I_{photo}$ is the captured fraction I_{photo}, and i_{photo} the photocurrent emitted by a single quantum well. From equation (3.21), we can write the following:

$$I_{photo} = i_{photo}/p_c \tag{3.22}$$

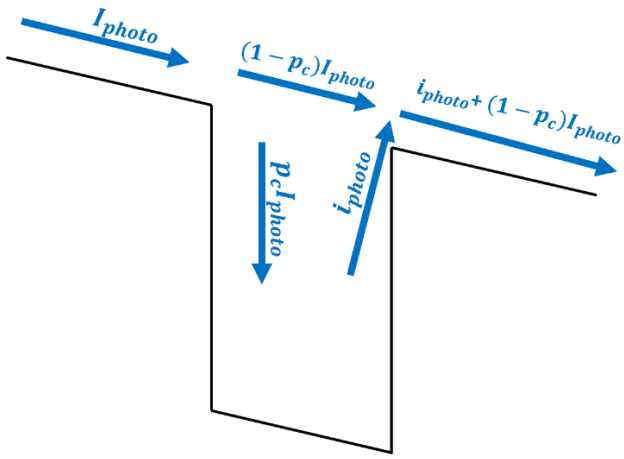

Figure 3.1. *A diagram depicting the carrier transportation through the active region of the QWIP.*

We are interested in finding an expression for the photocurrent I_{photo}, so we need first to find i_{photo}, then we can substitute into equation (3.22) to get I_{photo}. The photocurrent emitted by one quantum well is given as the electron charge multiplied by the number of excited electrons, divided by the escape time (the time taken by the electron

to escape from the well to the conduction band of the barrier material), which can be described by the following equation

$$i_{photo} = \frac{en_{ex}}{\tau_{esc}} \tag{3.23}$$

Now, in order to find n_{ex}, we consider the equation of the rate of excited electrons in the quantum well, as follows (Schneider & Liu, 2007)

$$\frac{\mathrm{d}n_{ex}}{\mathrm{d}t} = \phi\eta_1 - \frac{n_{ex}}{\tau_{esc}} - \frac{n_{ex}}{\tau_{relax}} \tag{3.24}$$

where ϕ is the number of incident photons per second, η_1 is absorption quantum efficiency of a single quantum well, τ_{esc} is the escape time and τ_{relax} is the relaxation time of the intersubband. Now, the number of excited electrons per unit time becomes constant when a steady state is reached, meaning that $\mathrm{d}n_{ex}/\mathrm{d}t = 0$, and by rearranging equation (3.24) we find that n_{ex} can be written as

$$n_{ex} = \frac{\tau_{esc}\tau_{relax}}{\tau_{esc}+\tau_{relax}}\phi\eta_1 \tag{3.25}$$

by substituting from equation (3.25) into equation (3.23), we find that the photocurrent emitted by one quantum well becomes:

$$\begin{aligned} i_{photo} &= \frac{e}{\tau_{esc}}\frac{\tau_{esc}\tau_{relax}}{\tau_{esc}+\tau_{relax}}\phi\eta_1 \\ &= \frac{\tau_{relax}}{\tau_{esc}+\tau_{relax}}e\phi\eta_1 \end{aligned} \tag{3.26}$$

$$= \frac{e\phi\eta p_e}{N}$$

where N is the number of quantum wells in the multiple quantum well structure, $\eta = N\eta_1$ is the total absorption quantum efficiency and p_e is the escape probability of an excited electron and can be described by the following equation:

$$p_e = \frac{\tau_{relax}}{\tau_{esc} + \tau_{relax}} \tag{3.27}$$

Now that we know i_{photo}, we can substitute the last line in equation (3.26) into equation (3.22) to get the equation of the photocurrent flowing through the active region of the device, as follow:

$$\begin{aligned} I_{photo} &= \frac{e\phi\eta}{N}\frac{p_e}{p_c} \\ &= e\phi\eta g_{photo} \end{aligned} \tag{3.28}$$

where g_{photo} is the photoconductive gain and it is described as in the following equation:

$$g_{photo} = \frac{p_e}{Np_c} \tag{3.29}$$

As mentioned earlier, p_c is the capture probability and it's given as (Schneider & Liu, 2007):

$$p_c = \frac{\tau_{trans}}{\tau_c + \tau_{trans}} \tag{3.30}$$

where τ_{trans} is the electron transit time, which the time taken by one electron to travel across one active region, and τ_c is the capture time. In bound to quasi-bound QWIPs, the escape time of excited electrons is much smaller than capture and relax time, and that's because once the electron reaches the quasi-bound state it can easily escape the well due to the quasi-bound state being very close to the top of the quantum well. In this case, we can say that $p_e \approx 1$ and $p_c \ll 1$, as the transit time is much smaller than the capture time.

3.4 Responsivity

Responsivity is a characteristic parameter of QWIPs that indicates how much photocurrent can be produced by the detector for a specific amount of incident photons, and its described as follows (Schneider & Liu, 2007):

$$R = \frac{I_{photo}}{\hbar\omega\phi} = \frac{e\phi\eta g_{photo}}{\hbar\omega\phi} = \frac{e\eta g_{photo}}{\hbar\omega} \tag{3.31}$$

ω is the angular frequency of the incident photons. Knowing that $\eta = N\eta_1$ and $g_{photo} \propto 1/N$, we find that the responsivity of the device doesn't depend on the number of quantum wells.

3.4. Dark current

Dark current refers to the current flowing in the detector when it is connected to external voltage bias but not exposed to electromagnetic radiation.

The three main contributors to the dark current in QWIPs are direct tunneling, thermo-assisted tunneling, and thermionic emission. Similar to the transport process of photocurrent across the active region, some of the dark current gets captured in the

quantum well and due to the three processes mentioned above, some electrons escape the quantum well and contribute to the total dark current with a current called i_{dark}, which is the dark current emitted from one quantum well, this process is illustrated in Figure (3.2).

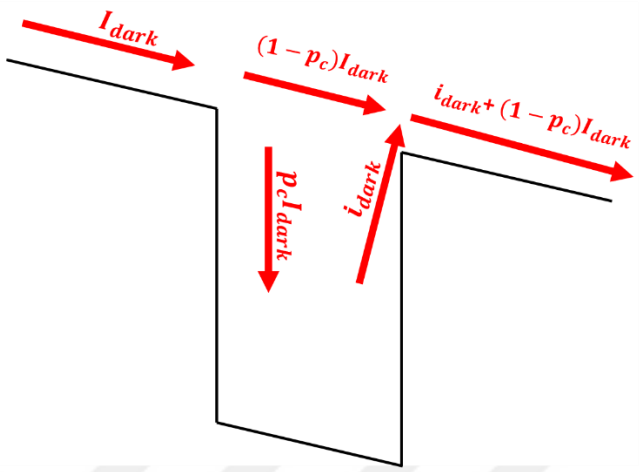

Figure 3.2. *Dark current flow across the active region of the QWIP.*

The process shown in Figure (3.2) can be described by the following equation:

$$I_{dark} = i_{dark} + (1 - p_c)I_{dark} \tag{3.32}$$

where p_c is capture probability and I_{dark} is the dark current flowing in three dimensions. From equation (3.32), we can write the following:

$$I_{dark} = \frac{i_{dark}}{p_c} \tag{3.33}$$

In order to find I_{dark}, there are two possible models to be used, namely the 3D Carrier Drift Model and the Emission-Capture Model (H. C. Liu, Steele, Buchanan, & Wasilewski, 1993). The 3D Carrier Drift Model targets to determine I_{dark} directly by treating the barrier material as a 3D bulk semiconductor, where the Emission-Capture Model focuses on finding i_{dark} then using equation (3.33) to find I_{dark} (Cao & Liu, 2011;Schneider & Liu, 2007). However, in this thesis, the 3D Carrier Drift Model will be used to find the expression of the dark current.

3.5.1 3D Carrier Drift Model

In this model, the dark current I_{dark} is written in terms of the 3D electron density in the barrier material and the drift velocity of the electrons, where the drift velocity is a function of the applied electric field. Hence, I_{dark} can be expressed as follows:

$$I_{dark} = eN_{3D}v(F)A \tag{3.34}$$

where F is the electric field strength, $v(F)$ is the drift velocity, N_{3D} is the 3D electron concentration in the barrier material and the area of the detector. The 3D electron concentration above the top of the quantum well can be determined as follows:

$$N_{3D} = \int_{E_c}^{\infty} g(E)f_{FD}(E)\mathrm{d}E \tag{3.35}$$

where $g(E)$ is the 3D density of states, $f_{FD}(E)$ is the Fermi-Dirac distribution, and E_c is the energy of the bottom of the conduction band of the barrier material, which is equivalent to the top of the quantum well, and we chose the zero energy to be at the bottom of the quantum well. The Fermi-Dirac distribution can be written as follows:

$$f_{FD}(E) = \frac{1}{1 + \exp\left[\frac{E - E_F}{k_B T}\right]} \tag{3.36}$$

where E is the energy of the electrons and E_F is the Fermi energy. On the other hand, the Density of States can be written as follows ("The Physics of Solids," 2008):

$$g(E) = \frac{\pi}{2}\left(\frac{8m^*}{h^2}\right)^{\frac{3}{2}}\sqrt{E - E_c} \tag{3.37}$$

Substituting from equation (3.36) and (3.37) into equation (3.35) results in the following:

$$N_{3D} = \frac{\pi}{2}\left(\frac{8m^*}{h^2}\right)^{\frac{3}{2}} \int_{E_c}^{\infty} \frac{\sqrt{E - E_c}}{1 + \exp\left[\frac{E - E_F}{k_B T}\right]} \mathrm{d}E$$

we can use the approximation $E - E_F \gg k_B T$, which means that we can write the previous equation as follows:

$$\begin{aligned}
N_{3D} &= \frac{\pi}{2}\left(\frac{8m^*}{h^2}\right)^{\frac{3}{2}} \int_{E_c}^{\infty} \sqrt{E - E_c} \exp\left[-\frac{E - E_F}{k_B T}\right] \mathrm{d}E \\
&= \frac{\pi}{2}\left(\frac{8m^*}{h^2}\right)^{\frac{3}{2}} \int_{E_c}^{\infty} \sqrt{E - E_c} \exp\left[-\frac{E - E_c}{k_B T} - \frac{E_c - E_F}{k_B T}\right] \mathrm{d}E \\
&= \frac{\pi}{2}\left(\frac{8m^*}{h^2}\right)^{\frac{3}{2}} \exp\left[-\frac{E_c - E_F}{k_B T}\right] \int_{E_c}^{\infty} \sqrt{E - E_c} \exp\left[-\frac{E - E_c}{k_B T}\right] \mathrm{d}E \\
&= \frac{\pi (k_B T)^{\frac{3}{2}}}{2}\left(\frac{8m^*}{h^2}\right)^{\frac{3}{2}} \mathrm{e}^{-\frac{E_c - E_F}{k_B T}} \int_{0}^{\infty} \sqrt{u}\, \mathrm{e}^{-u} \mathrm{d}u \\
&= \frac{\pi}{2}\left(\frac{8m^* k_B T}{h^2}\right)^{\frac{3}{2}} \mathrm{e}^{-\frac{E_c - E_F}{k_B T}} \frac{\sqrt{\pi}}{2} \\
&= \frac{1}{4}\left(\frac{2m^* k_B T}{\pi \hbar^2}\right)^{\frac{3}{2}} \mathrm{e}^{-\frac{E_c - E_F}{k_B T}} \\
&= 2\left(\frac{m^* k_B T}{2\pi \hbar^2}\right)^{\frac{3}{2}} \mathrm{e}^{-\frac{E_c - E_F}{k_B T}}
\end{aligned} \tag{3.38}$$

The drift velocity as a function of the strength of the applied electric field can be written as follows (Chuang, 2009):

$$v(F) = \frac{\mu F}{\sqrt{1 + \left(\frac{\mu F}{v_{sat}}\right)^2}} \tag{3.39}$$

where μ is the mobility of electrons and v_{sat} is the saturation drift velocity. Finally, the dark current can be obtained by substituting from the last line in equation (3.38) and equation (3.39) into equation (3.34):

$$I_{dark} = 2Ae \frac{\mu F \left(\frac{m^* k_B T}{2\pi\hbar^2}\right)^{\frac{3}{2}}}{\sqrt{1 + \left(\frac{\mu F}{v_{sat}}\right)^2}} \, \mathrm{e}^{-\frac{E_c - E_F}{k_B T}} \tag{3.40}$$

This model has been found to be in a good agreement with the experimental results at relatively low applied electric field (less than a few kV/cm) (Schneider & Liu, 2007).

3.5. Detectivity

Detectivity, D, is a significant parameter of characterization of QWIPs. The Specific detectivity of a QWIP, D^*, is defined as the detectivity D normalized by the square root of the area of the detector and the bandwidth, which can be described mathematically as follows:

$$\begin{aligned} D^* &= D\sqrt{A\Delta f} \\ &= \frac{R\sqrt{A\Delta f}}{i_n} \end{aligned} \tag{3.41}$$

where R is the responsivity and i_n is the noise current, and they both are given as follows (Schneider & Liu, 2007):

$$R = \frac{e\eta g_{noise}}{\hbar\omega} \tag{3.42}$$

$$i_n = \sqrt{4e g_{noise} I_{dark} \Delta f} \tag{3.43}$$

where $g_{noise} = 1 \,/\, Np_c$ is the noise gain and it equals the photoconductive gain when $p_e \approx 1$.

Substituting from (3.34), (3.42) and (3.43) into equation (3.41) results in the following:

$$\begin{aligned} D^* &= \frac{R\sqrt{A\Delta f}}{i_n} \\ &= \frac{e\eta g_{noise}}{\hbar\omega} \frac{\sqrt{A\Delta f}}{\sqrt{4e g_{noise} I_{dark} \Delta f}} \\ &= \frac{e\eta \sqrt{g_{noise}}}{\hbar\omega} \frac{\sqrt{A}}{\sqrt{4e^2 N_{3D} v\, A}} \\ &= \frac{\eta \sqrt{g_{noise}}}{2\hbar\omega \sqrt{N_{3D} v}} \\ &= \frac{\eta}{2\hbar\omega \sqrt{N_{3D} v}} \frac{1}{\sqrt{N p_c}} \end{aligned} \tag{3.44}$$

Taking into account that $p_c \approx \ \tau_{trans} \,/\, \tau_c$ for capture time much larger that transit time, and that the drift velocity is $v = L_p \,/\, \tau_{trans}$, where L_p is the width of the active region (the width of the well plus the width of the barrier), equation (3.44) becomes

$$D^* = \frac{\eta\sqrt{\tau_{trans}}}{2\hbar\omega\sqrt{N_{3D}L_p}}\frac{\sqrt{\tau}_c}{\sqrt{N\tau_{trans}}}$$

$$= \frac{\eta\sqrt{\tau}_c}{2\hbar\omega\sqrt{NL_p}}\frac{1}{\sqrt{N_{3D}}} \tag{3.45}$$

where N_{3D} is given in equation (3.38), and can be rewritten as follows (Schneider & Liu, 2007):

$$N_{3D} = 2\left(\frac{m^* k_B T}{2\pi\hbar^2}\right)^{\frac{3}{2}} \exp\left[-\frac{hc}{k_B T\lambda_c} + \frac{E_F}{k_B T}\right] \tag{3.46}$$

where $E_c = hc/\lambda_c$ and λ_c is the cutoff wavelength.

Increasing the detectivity of the device is something that must be kept in mind when designing the detector, equations (3.45) and (3.46) tell us that the parameters that the detectivity can be increased by increasing the absorption quantum efficiency and decreasing the capture probability (increasing τ_c), as well as by decreasing T and λ_c (Schneider & Liu, 2007). We know from equation (3.15) that $\eta \propto n_{2D}$, where n_{2D} is the area electron density in the quantum well, and it is given as follows ((Schneider & Liu, 2007)):

$$n_{2D} = \frac{mE_F}{\pi\hbar^2} \tag{3.47}$$

where E_F is Fermi's energy, and this means that $\eta \propto E_F$. But we also see that D^* is inversely proportional to the square root of N_{3D}, and $N_{3D} \propto e^{\frac{E_F}{k_B T}}$, which means that $D^* \propto \frac{1}{\sqrt{e^{\frac{E_F}{k_B T}}}}$. Hence, we can demonstrate the dependence of D^* on E_F in the following manner:

$$D^* \propto E_F e^{-\frac{E_F}{2k_BT}} \tag{3.48}$$

we can get the value of the Fermi energy that maximizes the detectivity by setting the first derivative of D^* to zero and solve the resultant equation for E_F, as follows:

$$\frac{\mathrm{d}D^*}{\mathrm{d}E_F} = \frac{\mathrm{d}}{\mathrm{d}E_F} E_F e^{-\frac{E_F}{2k_BT}} = 0$$

$$0 = e^{-\frac{E_F}{2k_BT}} - \frac{E_F}{2k_BT} e^{-\frac{E_F}{2k_BT}}$$

$$0 = 1 - \frac{E_F}{2k_BT}$$

solving the last equation gives the optimal Fermi's energy that would result in the larges detectivity, and the solution to this equation is as follows

$$E_F = 2k_BT \tag{3.49}$$

3.7. Absorption coefficient

There are multiple methods applied in the literature to derive the absorption coefficient (Eker, Hostut, Ergun, & Sokmen, 2006). However, here I will not go in the process of the derivation and will write the form of the two- dimensional absorption coefficients as used by many sources (Graf et al., 2009;Helm, 2000), which can be described by the following equation:

$$\alpha_{2D=} \frac{e^2 k_B T}{2\varepsilon_0 n_r c\hbar} \sum_{i,f} f_{if} \ln\left[\frac{1+\exp\left(\frac{E_F - E_i}{k_BT}\right)}{1+\exp\left(\frac{E_F - E_f}{k_BT}\right)}\right] \frac{\Delta E}{\pi(\hbar\omega - E_2 + E_1)^2 + \Delta E^2} \tag{3.50}$$

where n_r is the refractive index of the material, E_F is the Fermi energy, E_i is the energy of the ith state and E_f is the energy of the fth state and the other parameters have been defined in previous sections.

4. THZ QWP DESIGN AND SIMULATION

4.1. Potential profile calculation

The THz QWP studied in this thesis is based on a symmetric single quantum well model, where different structures have been studied in order to get the optimized design which gives the maximum absorption coefficient at 3THz. The Schrodinger equation for the system has been solved using the finite difference method and the results then used to find the Hartree potential by substituting for the wavefunction into Poisson's equation, and the resulting Hartree potential has been added to the original potential in the Schrodinger equation and the two equations have been solved self-consistently until the energies converged. The exchange correlation potential has also been added in the Schrodinger equation to get more accurate results. The effect of the exchange correlation potential is important to be considered when dealing with THz QWPs, as the Aluminum fraction in the barrier is usually in the range of 1.5 % to 4 % for this kind of detectors, which means that the depth of the quantum well is small and the difference between the energy states of the well is small as well, so any change in the potential can affect the peak absorption frequency.

The analysis of the structure has been done using a developed MATLAB simulation, and the simulation has been used to replicate some of the results published in the literature in order to make sure that it works fine. The first model for which the band diagram and absorption coefficient have been studied is **A0175** from (Graf et al., 2009). Figure (4.1) shows the band diagram of **A0175** produced by the MATLAB simulation with the exchange correlation potential (V_{xc}) not included, and Figure (4.2) shows the band diagram with V_{xc} included in the potential. The two diagrams show the ground and the first excited states, where the first excited state is almost aligned with the top of the well in Figure (4.1) and it is shifted below in Figure (4.2), which means that the structure

has changed from bound to quasi-bound system and became a bound to bound regime. The energy difference between the ground and first excited state changes as we include the Exchange correlation potential, where it is 20.13 meV before adding the V_{xc}, and it becomes 22.05 meV after including Vxc. This 2 meV change is significant for THz QWPs and can have a profound impact on the position of the peak absorption frequency. The results produced by the MATLAB simulation were found to be in a good agreement with the results in (Graf et al., 2009). Next, the absorption coefficient of the device has been plotted as a function of the incident THz radiation. Figure (4.3) depicts the normalized absorption coefficient with and without including the exchange correlation potential and the depolarization shift. When V_{xc} was not taken into account, the peak absorption frequency was found to be at f=4.9 THz, and after adding V_{xc} the peak absorption frequency shifted to f=5.3 THz. Furthermore, including the depolarization shift due to dynamic factors shifts the peak absorption frequency to f=5.7 THz, as shown in Figure (4.3).

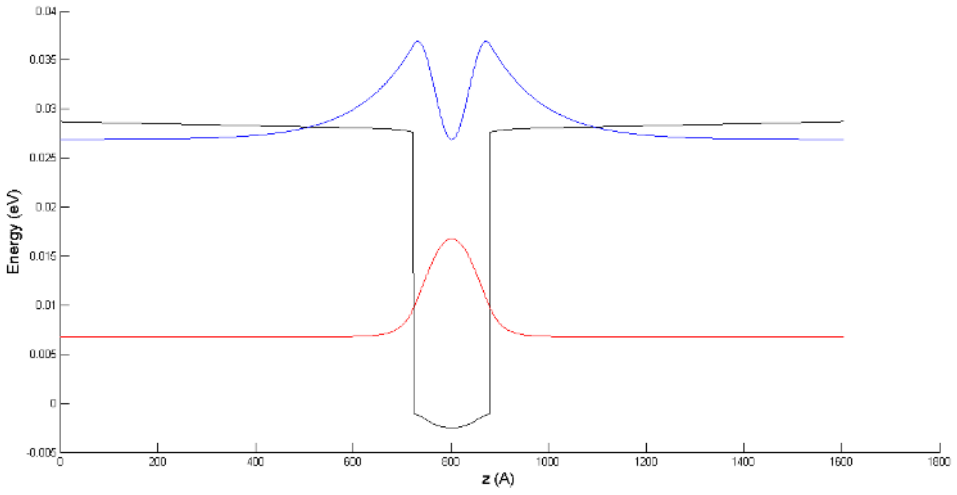

Figure 4.1. *The band diagram as given by the MATLAB simulation of model A0175 (Graf et al., 2009), without the effect of the exchange correlation potential.*

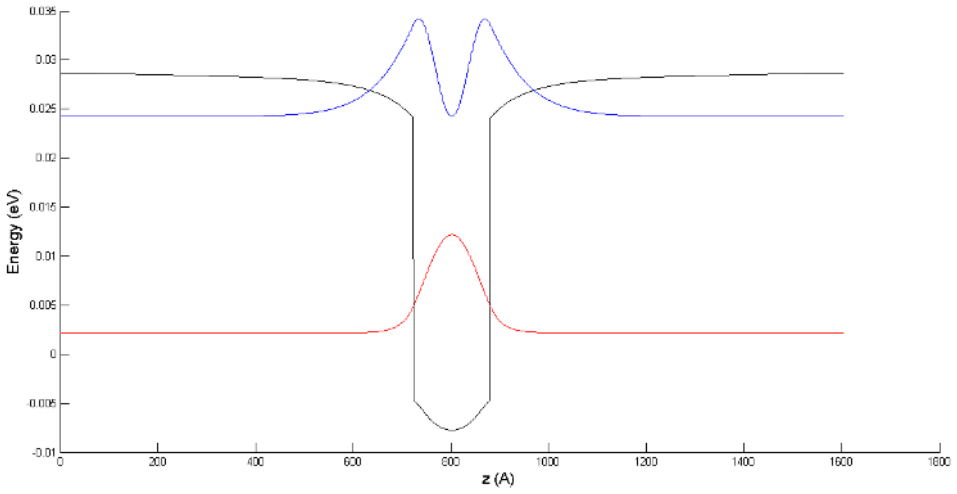

Figure 4.2. *The band diagram of model A0175 (Graf et al., 2009), after including the effect of the exchange correlation potential.*

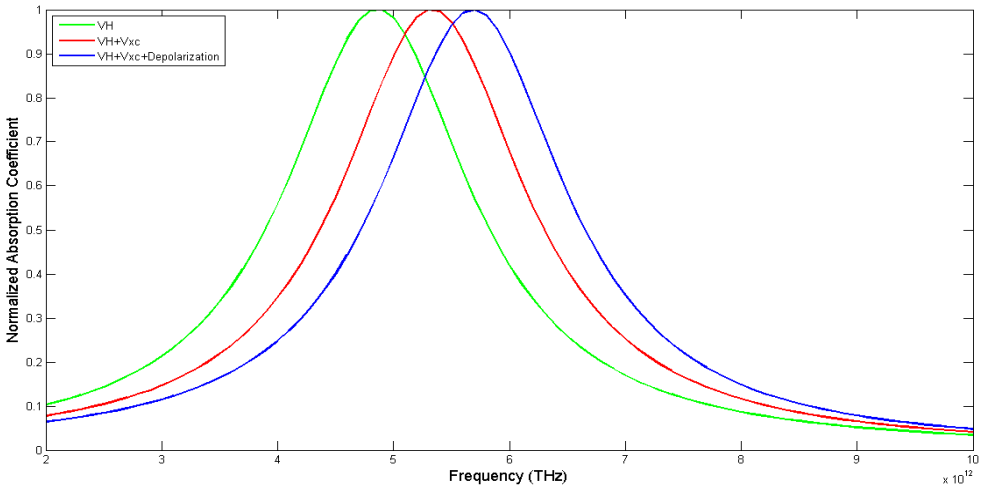

Figure 4.3. *The graph shows the normalized absorption coefficient for model A0175 from (Graf et al., 2009), with and without the consideration of the exchange correlation potential and depolarization shift.*

The developed MATLAB program has also been used to simulate two other THz QWPs reported in (Luo et al., 2006), the parameters of these devices and model A0175 are presented in Table (4.1). In all of the three models, the doping is inside the well over the center 100 A^0.

Table 4.1. *The table contains the parameters of model A0175(Graf et al., 2009), V265 and V267 (Luo et al., 2006).*

Model	L_w (A^0)	L_b (A^0)	Al (%)	n_{3D} (cm^{-3})	n_{2D} (cm^{-2})
A0175	155	702	3	1.5×10^{17}	1.5×10^{11}
V265	119	552	5	1×10^{17}	1×10^{11}
V267	221	951	1.5	3×10^{16}	3×10^{10}

Similar to what I did with A0175, Figure (4.4) shows the band diagram of V265 without including V_{xc} in the Schrodinger equation, and Figure (4.5) is the band diagram after adding V_{xc}. Figures (4.6) and (4.7) are describing the same thing but for model V267. The normalized absorption coefficient for models V265 and V267 with and without including the exchange correlation potential and the depolarization shift are shown in Figures (4.8) and (4.9) respectively.

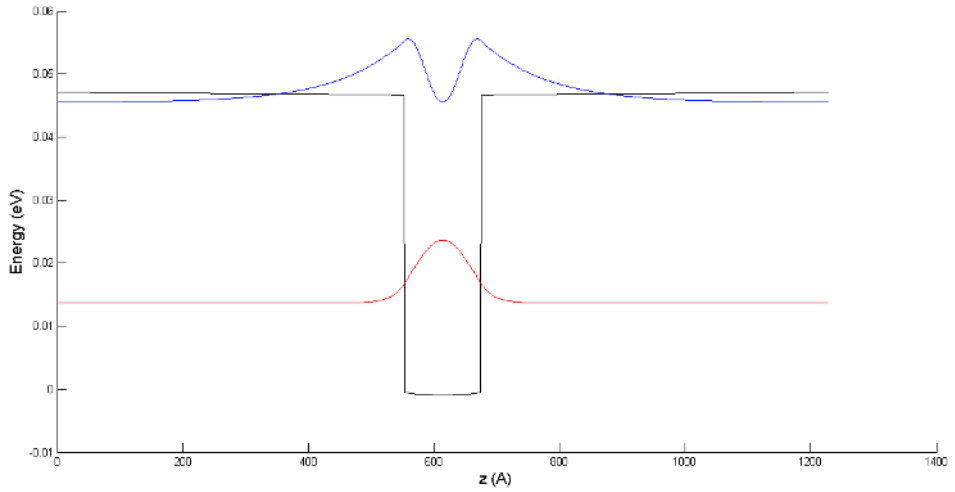

Figure 4.4. *The band diagram as given by the MATLAB simulation of model V265 (Luo et al., 2006), without the effect of* V_{xc}.

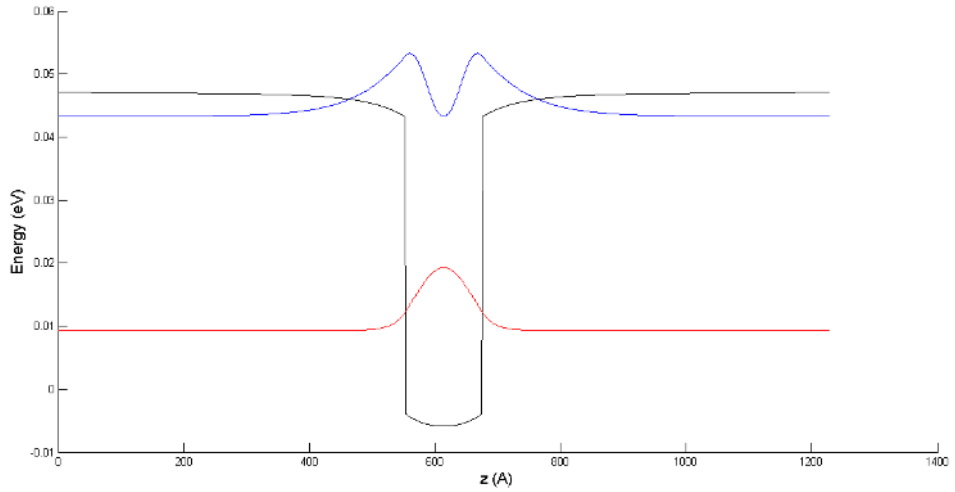

Figure 4.5. *The band diagram of model V265 (Luo et al., 2006), after including the effect of* V_{xc} .

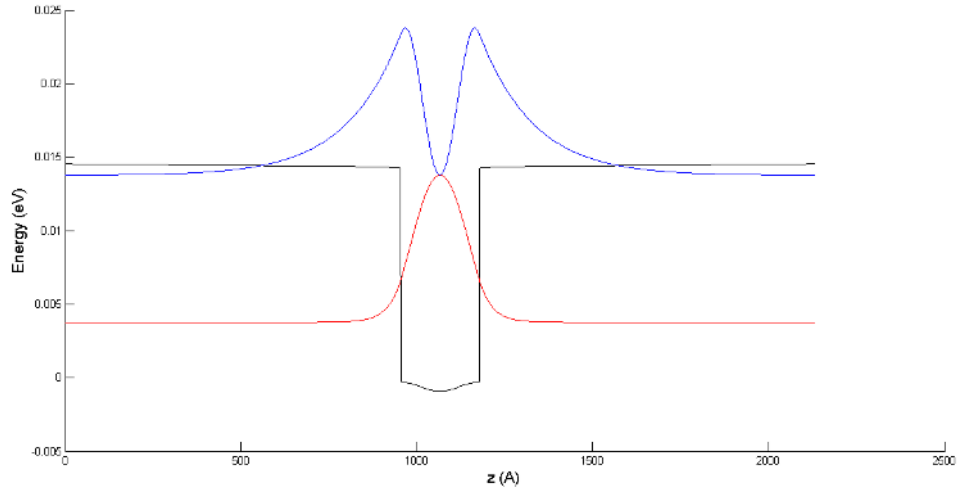

Figure 4.6. *The band diagram as given by the MATLAB simulation of model V267 (Luo et al., 2006), without the effect of* V_{xc}.

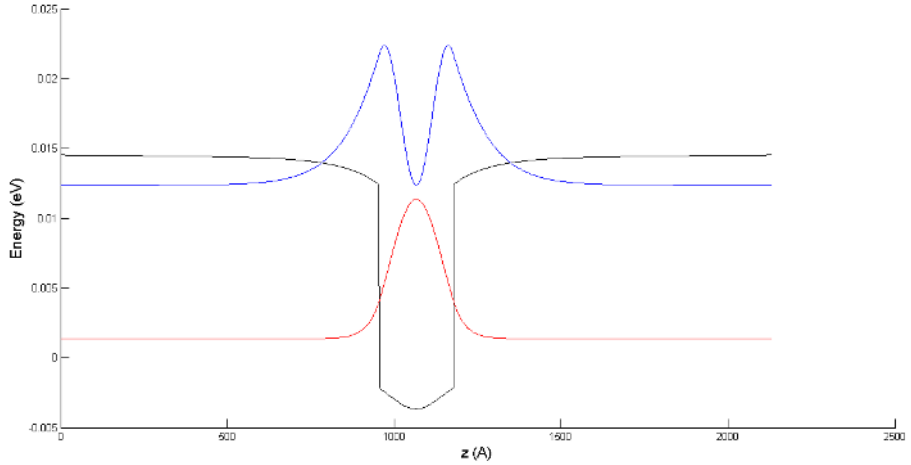

Figure 4.7. *The band diagram of model V267 (Luo et al., 2006), after including the effect of* V_{xc}.

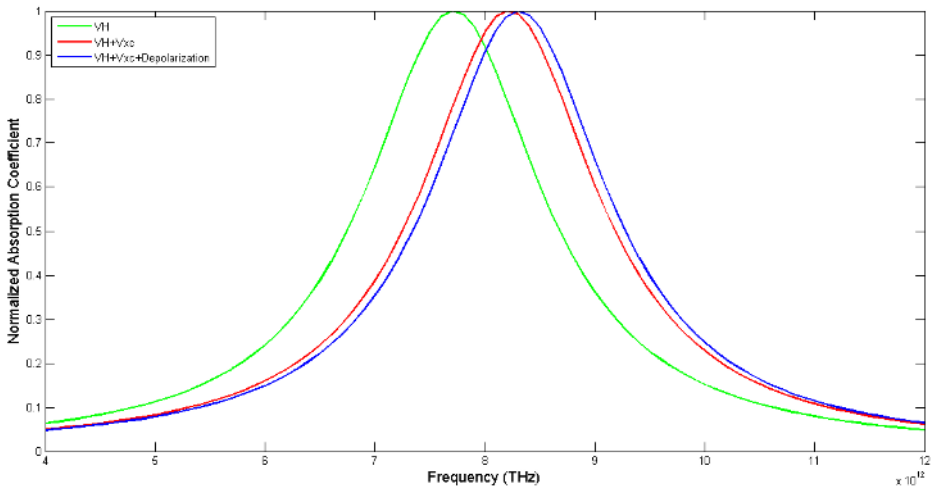

Figure 4.8. *The normalized absorption coefficient for model A265 from (Luo et al., 2006), with and without the consideration of the exchange correlation potential and depolarization shift.*

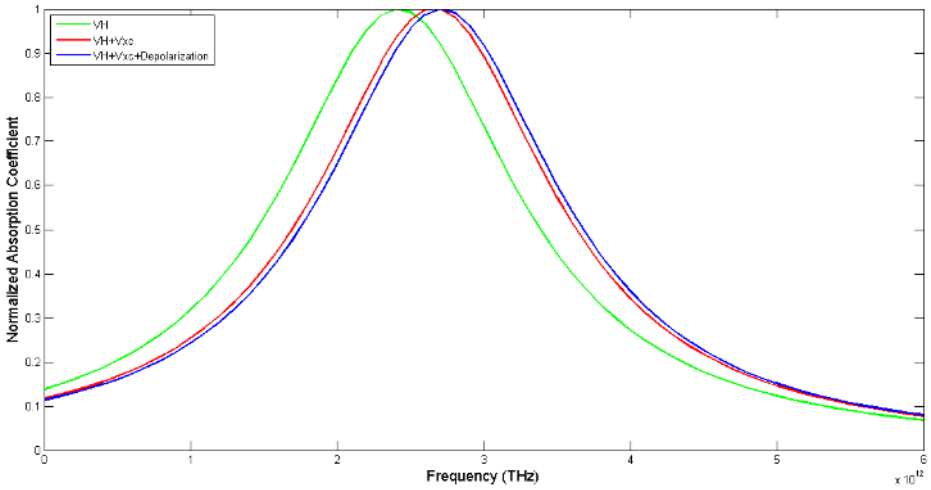

Figure 4.9. *The normalized absorption coefficient for model A267 from (Luo et al., 2006), with and without the consideration of the exchange correlation potential and depolarization shift.*

4.2. The design of our model

The target of the study is to get the optimal design that gives the highest absorption coefficient at a frequency of 3THz, meaning that we need to get the optimal design in which the energy difference between its ground and first excited state is about 12.4 meV. The main three parameters that controls this energy difference and the position of the energy levels are the width of the quantum well, the aluminum fraction, and the doping density. The plan is to run the simulation for different aluminum fractions and widths while keeping the doping density constant, and choosing the model that provides the highest absorption coefficient at 3 THz. The simulation will be run for aluminum fractions of 1.5%, 2%, 2.5%, and 3%, while the width will be changed from 100 A^{o} to 280 A^{o} with a step of 30 A^{o}. The doping density will be kept constant for all the models, and it will be $2 \times 10^{17} \mathrm{cm}^{-3}$, where both barriers will be doped over 20A^{o}, 10 A^{o} away from the well.

Figures (4.10), (4.11), (4.12) and (4.13) show the two-dimensional absorption coefficient for different quantum wells. The idea is to choose the design that provides the highest absorption peak close to 3THz. However, there is also another important condition that we want to be satisfied in our model, that is the first excited state being close to the top of the well, so we might find a design that gives the heights absorption peak at 3THz, but first excited energy is not very close to the top of the well, and in this

case we do further calculations and narrow the well in order to change the position of the first excited state and make it closer to the top.

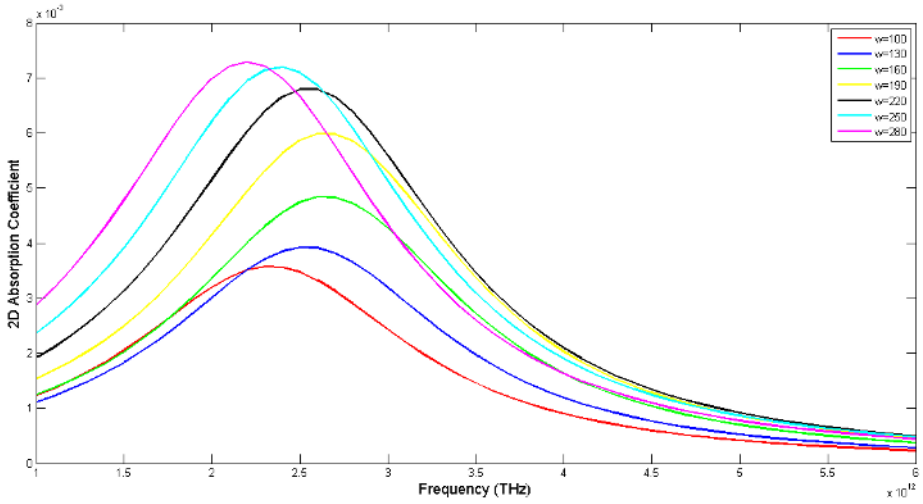

Figure 4.10. *The two-dimensional absorption coefficient for a single quantum well with aluminum fraction of 1.5% and different quantum well widths.*

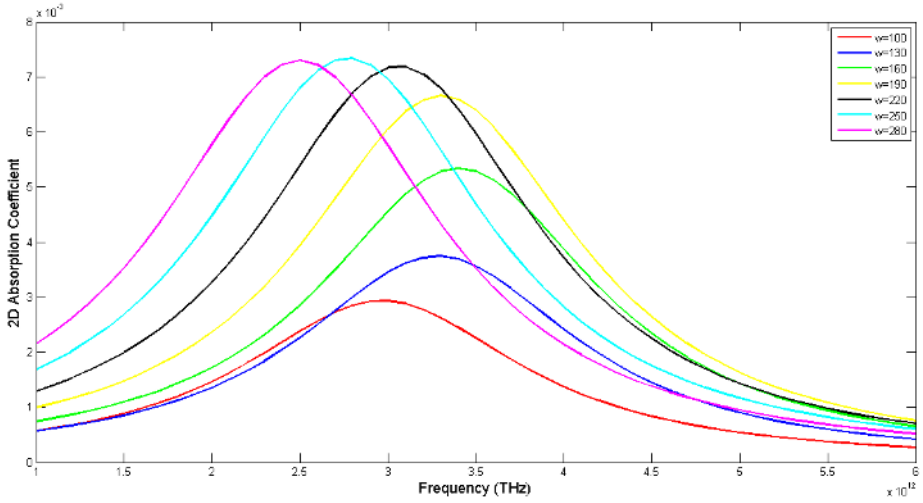

Figure 4.11. *The two-dimensional absorption coefficient for a single quantum well with aluminum fraction of 2 % and different quantum well widths.*

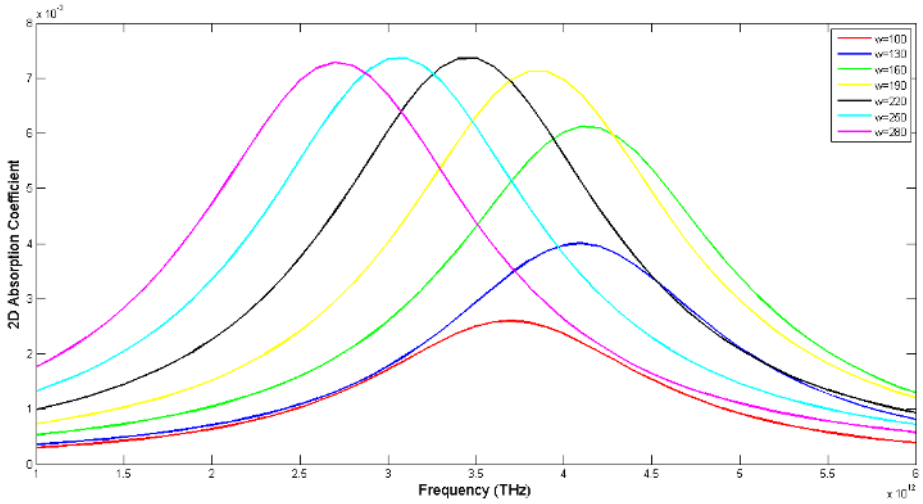

Figure 4.12. *The two-dimensional absorption coefficient for a single quantum well with aluminum fraction of 2.5 % and different quantum well widths.*

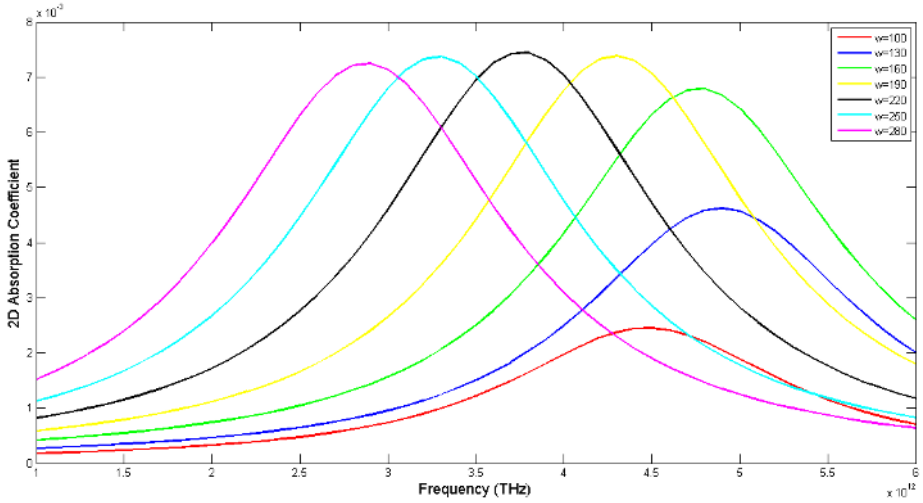

Figure 4.13. *The two-dimensional absorption coefficient for a single quantum well with aluminum fraction of 3 % and different quantum well widths.*

For the model with 1.5% aluminum fraction, we found that the frequencies at which the peak absorption occurs are as shown in table (4.2).

Table 4.2. *The peak frequencies for the model with aluminum fraction 1.5% at different quantum well widths.*

Well width (A^o)	Peak frequency (THz)
100	2.3
130	2.5
160	2.6
190	2.6
220	2.5
250	2.4
280	2.2

We notice that none of the peak frequencies shown in table (4.2) is close to 3THz, which leads us to conclude that the model with Al fraction 1.5% can't support peak absorption around 3 THz.

The peak frequencies for the models with 2%, 2.5% and 3% aluminum fraction, are shown in tables (4.3), (4.4) and (4.5) respectively.

Table 4.3. *The peak frequencies for the model with aluminum fraction 2% at different quantum well widths.*

Well width (A^o)	Peak frequency (THz)
100	3
130	3.3
160	3.4
190	3.3
220	3.1
250	3.8
280	3.5

Table 4.4. *The peak frequencies for the model with aluminum fraction 2.5% at different quantum well widths.*

Well width (A^o)	Peak frequency (THz)
100	3.7
130	4.1
160	4.1

190	3.9
220	3.5
250	3.1
280	3.7

Table 4.5. *The peak frequencies for the model with aluminum fraction 3% at different quantum well widths.*

Well width (A^o)	Peak frequency (THz)
100	4.5
130	4.9
160	4.8
190	4.3
220	3.8
250	3.3
280	2.9

By looking at tables (4.3), (4.4) and (4.5), we notice that we have four candidate models that can support peak absorption very close to 3 THz, and these models are shown in table (4.6)

Table 4.6. *The best candidate models that can support a peak absorption near 3 THz.*

Al fraction (%)	Well width (A^o)	Peak frequency (THz)
2	100	3
2	220	3.1
2.5	250	3.1
3	280	2.9

Here comes the other condition that we would like our model to have, namely that the first excited state of the well be aligned with the top of the well and that the well contain only two states. However, we found that a quantum well with aluminum fraction of 2% and width of 100 A^o has its first excited state above the top of the well, and the oscillator strength between the ground state and the first excited state is 0.4. This problem

can be solved by widening the well a little bit in order to shift the first excited state below and align it with the top. And we actually notice from table (4.3) that the peak frequency increases as the width of the well increases and converges near 3THz at a width of 220 A^o. However, at width of 220 A^o we find that the first excited state is not aligned with the top of the well, and by decreasing the well width to 205 A^o and decreasing the aluminum fraction to 1.9%, we succeeded to align the first excited state with the top of the well and getting the model to operate at a peak frequency of 3.1 THz.

The models with aluminum fractions of 2.5% and 3% are excluded because the first excited state can't be aligned with the top of the well and provide a peak frequency near 3THz at the same time.

Hence, we choose our model to have a width of 205 A^o and an aluminum fraction of 1.9%, $Al_{0.019}Ga_{0.981}As/GaAs$, with barriers of width of 750 A^o and with both barriers doped with a density of 2×10^{17} cm^{-3} over 20 A^o, 10 A^o away from the well. The band diagram and the absorption coefficient of this quantum well are shown in figures (4.11) and (4.12) respectively.

After getting the optimal model, the dark current of this model need to be simulated and studied, and a MATLAB simulation is developed for this purpose and the result of the simulation will be presented in the next section.

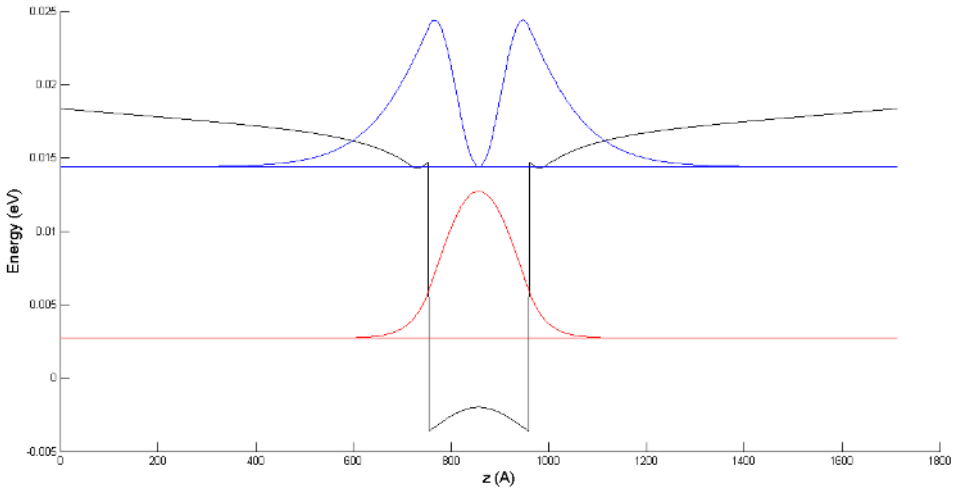

Figure 4.14. *The band diagram of the chosen model that operates at a peak frequency of 3.1 THz.*

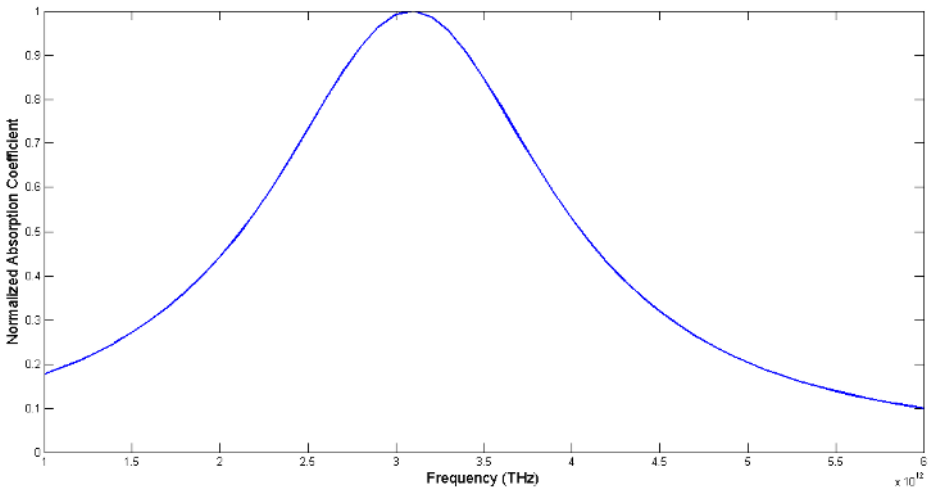

Figure 4.15. *The normalized absorption coefficient for the chosen model, with the consideration of the exchange correlation potential and depolarization shift.*

4.3. Dark current simulation

A dark current simulation has been developed using MATLAB based on the 3D Carrier Drift Model, the simulation has been tested by applying it for two models that have been previously reported at different temperatures, namely V267 and V266 (Luo et al., 2006). The results of the simulation for V267 were found to be in good agreement with the experimental results reported in (Tan et al., 2009). For V266, the simulation has been run for positive bias at different temperatures and compared with the results shown in Fig. 4.25 in decades (Schneider & Liu, 2007), the results of the simulation were also found to be in the same magnitude for temperatures larger than 9K. The mobility values were extracted from Figure 5 in (Tan et al., 2009). The results of our simulation along with the previously reported results are shown in figures (4.16) and (4.17).

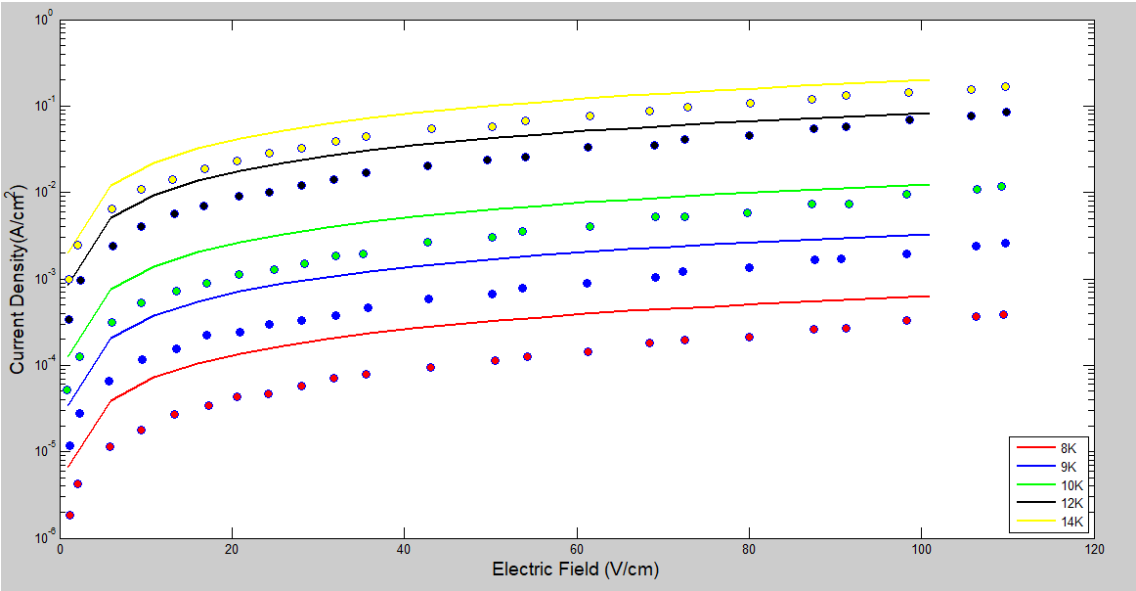

Figure 4.16. *Dark current simulation results (solid lines) and experiment results obtained from (Tan et al., 2009) (dots) of dark current (V267).*

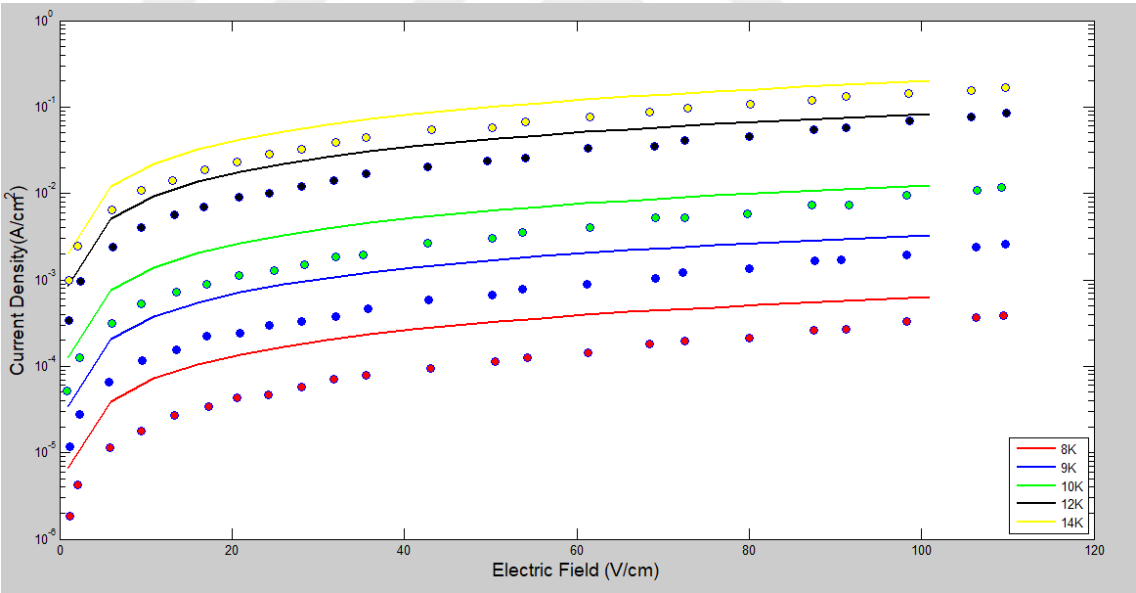

Figure 4.17. *Dark current simulation results (solid lines) and experiment results obtained from (Schneider & Liu, 2007) (dashed lines) of dark current (V266).*

Now that we have established that the simulation gives results that can be in a good agreement with the experimental data, we can run the simulation for our device for a positive bias of electric field from 1 to 201 V/cm at temperatures $T = 7,9,11,13,15$ K. The result of the simulation is shown in figure (14.18).

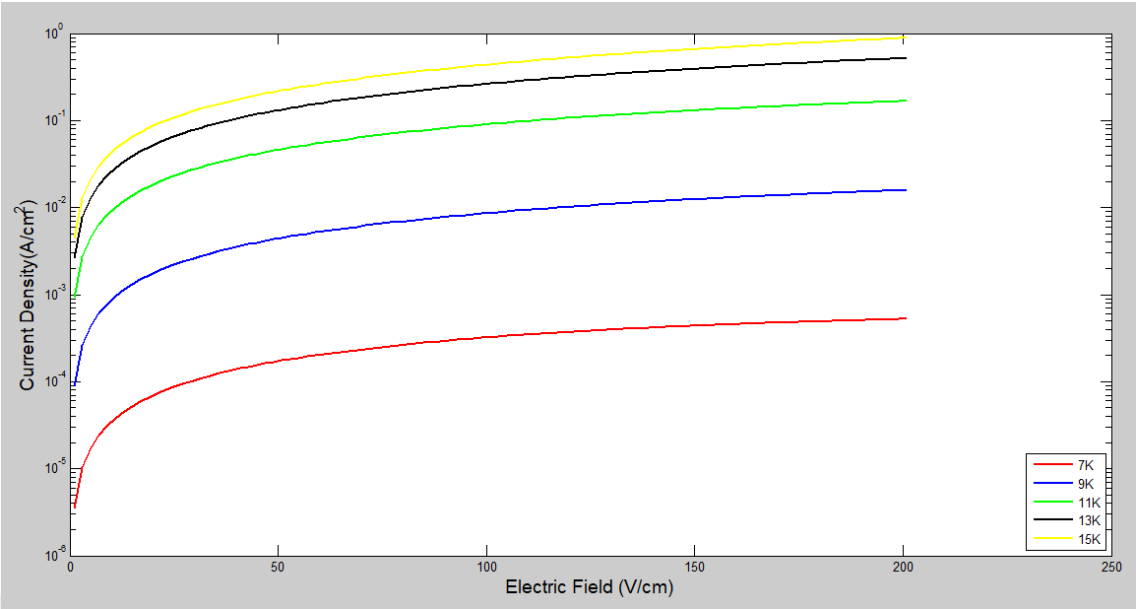

Figure 4.18. *Dark current simulation results for the THz QWP device developed in this thesis.*

We notice that the dark current increases dramatically as the temperatures increases from 7K to 11K, then then it increases at a slower for temperatures higher than 11K.

4.4. Conclusion

In this chapter, simulation models have been developed using MATLAB to get the optimal modulation doped structure of THz QWP that operates at a peak frequency around 3 THz, its dark current and absorption coefficient. The simulations models have been tested by replicating results that have been reported and published previously, and the results of the simulations were found to be in a good agreement with the published results. The optimal structure was found to operate at a peak frequency of 3.1 THz and the design was chosen to be based on bound to quasibound intersubband transitions.

For future work, the device can be fabricated in the lab and more characterization can be done, then experimental results can be compared with the simulation results reported in this thesis.

REFERENCES

Boltaev, A., Loiko, N., Rzaev, M., & Sibeldin, N. (2000). External Electric Field Effect on Energy Level Positions in a Quantum Well. *Proceedings of the 8th International Symposium Nanostructures: Physics and Technology*.

Bosco, L., Franckié, M., Scalari, G., Beck, M., Wacker, A., & Faist, J. (2019). Thermoelectrically cooled THz quantum cascade laser operating up to 210 K. *Applied Physics Letters, 115*(1), 010601. doi:10.1063/1.5110305

Brillson, L. (2016). Semiconductor Heterojunctions. In (pp. 223-248).

Cao, J. C., & Liu, H. C. (2011). Chapter 4 - Terahertz Semiconductor Quantum Well Photodetectors. In S. D. Gunapala, D. R. Rhiger, & C. Jagadish (Eds.), *Semiconductors and Semimetals* (Vol. 84, pp. 195-242): Elsevier.

Castellano, F., Iotti, R. C., & Rossi, F. (2008). Improving the operation temperature of semiconductor-based terahertz photodetectors: A multiphoton design. *Applied Physics Letters, 92*(9), 091108. doi:10.1063/1.2890167

Chuang, S. L. (2009). *Physics of Photonic Devices*: Wiley Publishing.

Dem'yanenko, M. A., Esaev, D. G., Toropov, A. I., Valisheva, N. A., Dvoretsky, S. A., Dmitriev, D. V., . . . Zhuravlev, K. (2018). AlGaAs/GaAs Quantum Well Infrared Photodetectors. In *Two-dimensional Materials for Photodetector*.

Eker, S. U., Hostut, M., Ergun, Y., & Sokmen, I. (2006). A new approach to quantum well infrared photodetectors: Staircase-like quantum well and barriers. *Infrared Physics & Technology, 48*(2), 101-108. doi:https://doi.org/10.1016/j.infrared.2005.04.009

Enderlein, R., Holz, T., & Gondar, J. L. (1989). The Quantum Well in an Electric Field A Density of States Approach. *physica status solidi (b), 156*(1), 259-273. doi:10.1002/pssb.2221560126

Ferré, S., Razavipour, S. G., & Ban, D. (2013). Terahertz quantum well photodetectors with improved designs by exploiting many-body effects. *Applied Physics Letters, 103*. doi:10.1063/1.4819036

Graf, M., Dupont, E., Luo, H., Haffouz, S., Wasilewski, Z. R., Spring Thorpe, A. J., . . . Liu, H. C. (2009). Terahertz quantum well infrared detectors. *Infrared Physics & Technology, 52*(6), 289-293. doi:https://doi.org/10.1016/j.infrared.2009.05.034

Graf, M., Scalari, G., Hofstetter, D., Faist, J., Beere, H., Linfield, E., . . . Davies, G. (2004). Terahertz range quantum well infrared photodetector. *Applied Physics Letters, 84*(4), 475-477. doi:10.1063/1.1641165

Guo, X. G., Cao, J. C., Zhang, R., Tan, Z. Y., & Liu, H. C. (2013). Recent Progress in Terahertz Quantum-Well Photodetectors. *IEEE Journal of Selected Topics in Quantum Electronics, 19*(1), 8500508-8500508. doi:10.1109/JSTQE.2012.2201136

Haug, H. Theory of Optical Properties of Quantum Wells, Wires and Dots. In (pp. 379-406).

Helm, M. (2000). *Intersubband Transition in Quantum Wells: Physics and Device Applications I. Semiconductors and Semimetals, vol. 62, ch. 1.*: Academic Press.

Jia, J. Y., Wang, T., Zhang, Y., & Schneider, H. (2015). High-Temperature Photon-Noise-Limited Performance Terahertz Quantum-Well Photodetectors. *Terahertz Science and Technology, IEEE Transactions on, 5*, 715-724. doi:10.1109/TTHZ.2015.2453632

Lee, Y.-S. (2009). *Principles of Terahertz Science and Technology*.

Levine, B. F. (1993). Quantum-well infrared photodetectors. *Journal of Applied Physics, 74*(8), R1-R81. doi:10.1063/1.354252

Levine, B. F., Choi, K. K., Bethea, C. G., Walker, J., & Malik, R. J. (1987). New 10 μm infrared detector using intersubband absorption in resonant tunneling GaAlAs superlattices. *Applied Physics Letters, 50*(16), 1092-1094. doi:10.1063/1.97928

Liboff, R. L. (2003). *Introductory Quantum Mechanics, fourth edition*.

Liu, H. C. (1993). Dependence of absorption spectrum and responsivity on the upper state position in quantum well intersubband photodetectors. *Journal of Applied Physics, 73*(6), 3062-3067. doi:10.1063/1.352989

Liu, H. C., Song, C. Y., SpringThorpe, A. J., & Cao, J. C. (2004). Terahertz quantum-well photodetector. *Applied Physics Letters, 84*(20), 4068-4070. doi:10.1063/1.1751620

Liu, H. C., Steele, A. G., Buchanan, M., & Wasilewski, Z. R. (1993). Dark current in quantum well infrared photodetectors. *Journal of Applied Physics, 73*(4), 2029-2031. doi:10.1063/1.353146

Liu, X.-h., Liao, K.-s., Zhou, X.-h., Li, Z.-f., & Li, N. (2013, August 01, 2013). *A 46μm AlGsAs/GaAs terahertz quantum-well infrared photodetector.* Paper presented at the Society of Photo-Optical Instrumentation Engineers (SPIE) Conference Series.

Lundstrom, M. S. (1995). Notes on Heterostructure Fundamentals. In.

Luo, H., Liu, H. C., Song, C. Y., Wasilewski, Z. R., SpringThorpe, A. J., & Cao, J. C. (2006). *Terahertz quantum well photodetectors* (Vol. 6308): SPIE.

Mittleman, D. M. (2017). Perspective: Terahertz science and technology. *Journal of Applied Physics, 122*(23), 230901. doi:10.1063/1.5007683

Okhovat-Alavian, S. M. J., Afzali-Kusha, A., & Kamarei, M. (2001). Intersubband transitions in conduction-band quantum wells. *12*, 53-62.

Ozturk, E., Ergun, Y., Sari, H., & Sokmen, I. (2000). Electronic subband of single Siδ-doped GaAs structures. *Superlattices and Microstructures, 28*(1), 35-45. doi:https://doi.org/10.1006/spmi.2000.0848

Pawar, A. Y., Sonawane, D. D., Erande, K. B., & Derle, D. V. (2013). Terahertz technology and its applications. *Drug Invention Today, 5*(2), 157-163. doi:https://doi.org/10.1016/j.dit.2013.03.009

. The Physics of Solids. (2008). In *The Materials Science of Semiconductors* (pp. 21-72). Boston, MA: Springer US.

Ridley, O. K. (2013). *Quantum Processes in Semiconductors*.

Rogalski, A. (2017). Terahertz detectors. In.

Schneider, H., & Liu, H. C. (2007). *Quantum well infrared photodetectors : physics and applications*: Springer.

Shankar, R. (1994). Principles of Quantum Mechanics, second edition.

Tan, Z. Y., Guo, X. G., Cao, J. C., Li, H., Wang, X., Feng, S. L., . . . Liu, H. C. (2009). Temperature dependence of current–voltage characteristics of terahertz quantum-well photodetectors. Semiconductor Science and Technology, 24(11), 115014. doi:10.1088/0268-1242/24/11/115014

Zhang, R., Shao, D. X., Fu, Z. L., Wang, H. X., Zhou, T., Tan, Z. Y., & Cao, J. C. (2017). Terahertz Quantum Well Photodetectors With Metal-Grating Couplers. IEEE Journal of Selected Topics in Quantum Electronics, 23(4), 1-7. doi:10.1109/JSTQE.2016.2608618

Zhang, S., Wang, T., Hao, M. R., Yang, Y., Zhang, Y., & Liu, H. (2013). Terahertz quantum-well photodetectors: Design, performance, and improvements. Journal of Applied Physics, 114, 194507-194507. doi:10.1063/1.4826625

CURRICULUM VITAE

ORCID ID: 0000-0002-1795-4420

Personal Information

Name/Surname	:	MAHMOUD H.M. ALMASSRI
Nationality	:	Palestinian
Date of Birth	:	22.08.1993
Place of Birth	:	Palestine
Gender	:	Male

Educational Background

2018-2020	:	MSc. In Physics at Eskişehir Teknik Üniversitesi, Turkey
2012-2016	:	BSc. In Physics at Islamic University of Gaza, Palestine.

Experience

2016-2017	:	Teaching Assistant at Islamic university of Gaza, Palestine

Languages

Arabic	:	Mother tongue
English	:	Very Good
Turkish	:	Good
Hebrew	:	Beginner